Nanoscale

REVIEW

View Article Online
View Journal | View Issue

Cite this: *Nanoscale*, 2023, **15**, 9605

Carbon-based single-atom catalysts: impacts of atomic coordination on the oxygen reduction reaction

Zhiwen Kang,[a] Xiaochen Wang,[a] Dan Wang,[a] Bing Bai,[b] Yafei Zhao, [a] Xu Xiang, [c] Bing Zhang *[a] and Huishan Shang *[a]

Slow oxygen reduction reaction (ORR) kinetics is the main factor restricting the development of fuel cells and metal–air batteries. Carbon-based single-atom catalysts (SACs) have the advantages of high electrical conductivity, maximal atom utilization, and high mass activity, thus showing great potential in exploring low-cost and high-efficiency ORR catalysts. For carbon-based SACs, the defects in the carbon support, the coordination of non-metallic heteroatoms, and the coordination number have a great influence on the adsorption of the reaction intermediates, thus significantly affecting the catalytic performance. Consequently, it is of vital importance to summarize the impacts of atomic coordination on the ORR. In this review, we focus on the regulation of the central atoms and coordination atoms of carbon-based SACs for the ORR. The survey involves various SACs, from noble metals (Pt) to transition metals (Fe, Co, Ni, Cu, *etc.*) and major group metals (Mg, Bi, *etc.*). At the same time, the influence of defects in the carbon support, the coordination of non-metallic heteroatoms (such as B, N, P, S, O, Cl, *etc.*), and the coordination number of the well-defined SACs on the ORR were put forward. Then, the impact of the neighboring metal monomers for SACs on the ORR performance is discussed. Finally, the current challenges and prospects for the future development of carbon-based SACs in coordination chemistry are presented.

Received 20th March 2023,
Accepted 27th April 2023

DOI: 10.1039/d3nr01272g

rsc.li/nanoscale

1. Introduction

In facing the over-consumption of fossil fuels and the ensuing energy and environmental crisis, it is of vital importance to develop sustainable energy technologies.[1–7] Proton exchange membrane fuel cells (PEMFCs) and metal–air batteries stand out among the various new energy sources due to their high energy density, environment friendliness, and resource-renewing ability.[8–14] The ORR is a key process in fuel cells and metal–air batteries, and their overall efficiency is severely limited by the slow ORR.[15–20] Pt/C catalysts are the currently used commercial ORR catalysts. However, their high cost and unstable nature have severely hampered their industrial application.[21–26] Therefore, new cost-effective and stable electrocatalysts must be developed to lower the reaction energy barrier, accelerate the reaction rate and eventually increase the efficiency of the energy conversion.

In order to improve the catalytic activity of ORR catalysts, it is necessary to study the reaction mechanism of the ORR process. In 1976, Wroblowa proposed the most effective explanation of the complex ORR step mechanism.[27] The ORR process can proceed through two reaction paths, one through a four-electron ($4e^-$) reaction path to produce OH^- (in alkaline medium) and H_2O (in acidic medium), and the other through a two-electron ($2e^-$) reaction path to produce HO_2^- (in alkaline medium) and H_2O_2 (in acidic medium).[28] No hydrogen peroxide is produced in the $4e^-$ reaction, avoiding adverse effects on the catalyst, and the current efficiency is higher, which is ideal for the cathodic reduction reaction of fuel cells. Therefore, it is preferable for the oxygen reduction reaction to proceed by a $4e^-$ reaction mechanism.

In the past few decades, SACs have been deeply explored by researchers due to their advantages of cost-effectiveness, maximal atom utilization, and high intrinsic activity.[29–31] So far, this has become one of the most popular research areas in the field of electrocatalysis.[32–35] SACs consist of metal single atoms bonded to atoms on carriers with an unsaturated coordination configuration.[36–39] The binding energy of the chemical intermediates can be greatly affected by the coordination structure.[40] So, small variations in ligand structure have an impact on the performance of the catalysts, even if they are similar-structure catalysts. Coordination engineering is achieved mainly through the modulation of the active central atoms, the distribution of defects in the carriers, and the regu-

[a]*School of Chemical Engineering, Zhengzhou University, Zhengzhou, 450001, P. R. China. E-mail: zhangb@zzu.edu.cn, shanghs@zzu.edu.cn*
[b]*Key Lab For Special Functional Materials, Ministry of Education, School of Materials, Henan University, Kaifeng, 100029, China*
[c]*State Key Laboratory of Chemical Resource Engineering, Beijing University of Chemical Technology, Beijing 100029, China*

lation of the coordination atoms. Accurate and advanced characterization tools such as synchrotron radiation X-ray absorption fine structure (XAFS) and density functional theory (DFT) calculations also play important roles in the modulation of the coordination patterns.[41–44] Up to now, many excellent electrocatalysts for the ORR have been designed and synthesized. Many excellent reviews have provided comprehensive summaries of various approaches to improve ORR activity.[45–48] However, most of these are expounded from the macroscopic aspects such as the synthesis method, selection of the active center metal, catalyst morphology, *etc*. In-depth coordination engineering research studies and summaries are rare.

In this review, we comprehensively summarize and discuss the effects of coordination engineering for SACs on ORR performance. Firstly, we discuss the typical synthetic techniques and structural features of carbon-based SACs. Then, the types of central atom in SACs are summarized, which involve the most active noble metal Pt and a series of transition metals with the most development potential, as well as the seldom investigated group metals (Fig. 1). Especially, the effect of defects in the carrier, the coordination of non-metallic heteroatoms (such as B, N, P, S, O, Cl, *etc*.), and the coordination environment of the SACs on the reaction path, reduction products, ORR catalytic activity, and durability are discussed. In addition to this, we also summarize the influence of adjacent metal monomers for SACs on ORR performance (Fig. 2). Finally, a brief outlook on the current challenges and prospects of SACs for ORR reactions is also presented.

2. Synthesis strategies and structural characteristics

For carbon-based SACs, the synthesis methods directly determine the density of active sites and the coordination environment. In addition, the proper application of structural characteristics provides a deeper understanding of the mechanism. In this section, we summarize the synthesis strategies and structural characteristics of carbon-based SACs.

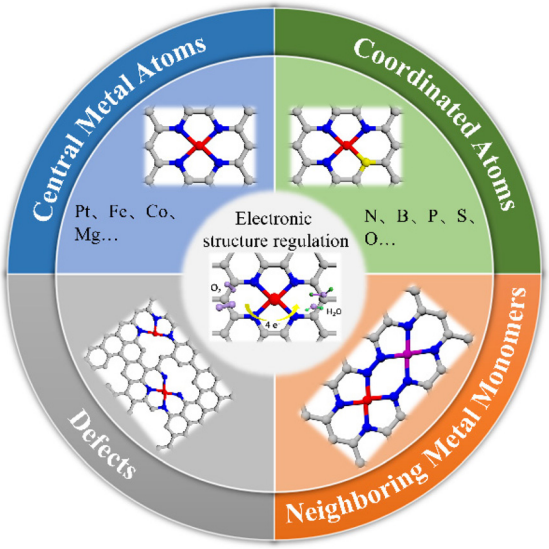

Fig. 2 The overview of carbon-based SACs electrocatalysts for the ORR.

2.1 Synthesis strategies

Precise control of the synthesis process is the basis for the development of efficient catalysts.[49–51] However, due to the weak interaction with the carbon carrier, the metal atoms are prone to migration or agglomeration.[46] Therefore, it is important to explore the synthesis strategy. The wet chemistry and high-temperature pyrolysis strategies are two of the most prevalent synthesis strategies for carbon-based SACs. Therefore, we mainly focus on these two synthesis strategies in this section.

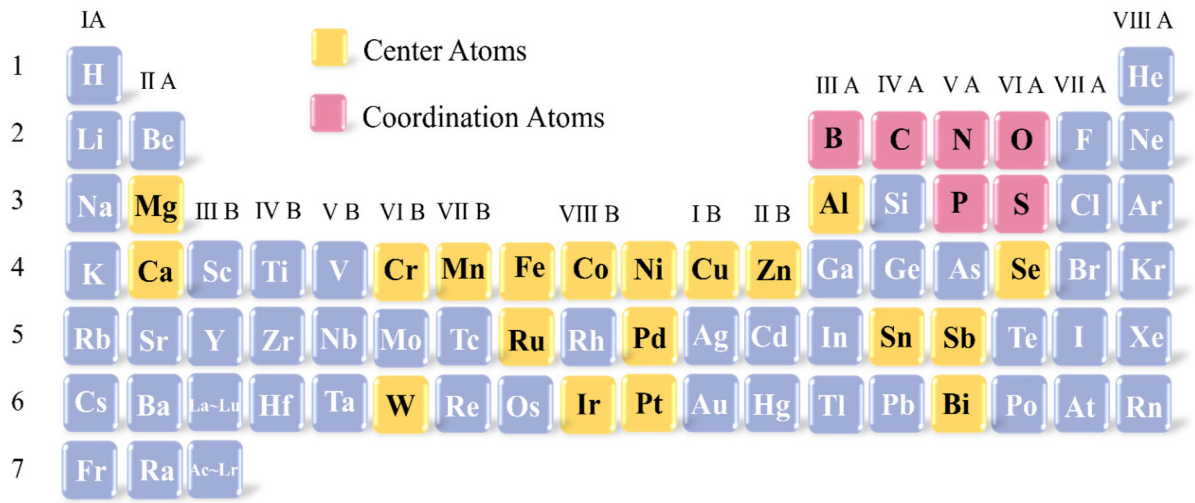

Fig. 1 Summary of elements in carbon-based SACs for the electrochemical ORR.

2.1.1 Wet chemistry strategy. The wet chemical method has become a common method for the preparation of SACs due to its simple and mild operation conditions.[29,52–54] For example, Wu *et al.*[55] polymerized *o*-phenylenediamine (*o*PD) in a solution containing $K_3[Fe(CN)_6]$ and $(NH_4)_2S_2O_8$ by a wet chemistry strategy, and then obtained Fe_1/N,S-PC by high temperature pyrolysis (Fig. 3a). Due to the coordination polymer strategy, the Fe_1/N,S-PC catalyst exhibited an excellent ORR performance with an $E_{1/2}$ of 0.904 V (Fig. 3b), high methanol tolerance and stability. Structural characterization and DFT calculations indicate that the excellent ORR activity is due to the dispersed Fe–N_4 active sites and the enhanced oxygen adsorption of N,S heteroatoms. As shown in Fig. 3c, Zhong *et al.*[56] successfully synthesized Co@NCB by the impregnation method. They first mixed cobalt acetate with pre-prepared resorcinol formaldehyde and then subjected it to pyrolysis. In Co@NCB, cobalt was present in the form of both Co nanoparticles and CoN_4. The obtained catalyst showed a better ORR activity than that of commercial Pt/C.

2.1.2 Thermal pyrolysis strategy. High-temperature pyrolysis strategy is another commonly used method in the preparation of SACs. Main-group (s- and p-block) metals are generally regarded as catalytically inactive due to the delocalized s/p-band. However, recent studies have shown that the main group metals can also be excellent ORR catalysts by optimization of the synthesis method. Wang *et al.*[57] obtained Sb SACs with Sb–N_4 active sites by the pyrolysis of Sb/ZIF-8 at 1000 °C for 2 h under a nitrogen atmosphere (Fig. 3d). The half-wave potential of the obtained Sb SAC was 0.86 V with excellent stability. The zinc–air battery prepared with Sb SAC as the air cathode also showed an excellent performance with a power density of 184.6 mW cm^{-2} and a specific capacity of 803.5 mA h g^{-1}.

2.1.3 Other synthetic strategies. Other effective ways for synthesizing carbon-based SACs exist in addition to the two more prevalent synthesis methods listed above. Recently, Wang *et al.*[58] prepared Sn SACs by the dual melting salt-mediated soft template method in Fig. 3e. By adjusting the pore structure, highly exposed Sn active centers were obtained, resulting in excellent ORR activity. The half-wave potentials in acidic and alkaline media were 0.816 and 0.905 V, respectively. In Fig. 3f, Dong *et al.*[59] used electrospinning to prepare polyacrylonitrile (PAN) nanofibers containing hemin (chloropropophyrin IX iron(III), TMMs), which is also a novel method. After subsequent pyrolysis, Fe–N-CNFs catalyst were obtained. PAN can effectively avoid the agglomeration of Fe, thus obtaining evenly dispersed Fe–N_4 active sites. Therefore, it exhibited excellent ORR activity in an acidic or alkaline solution. In

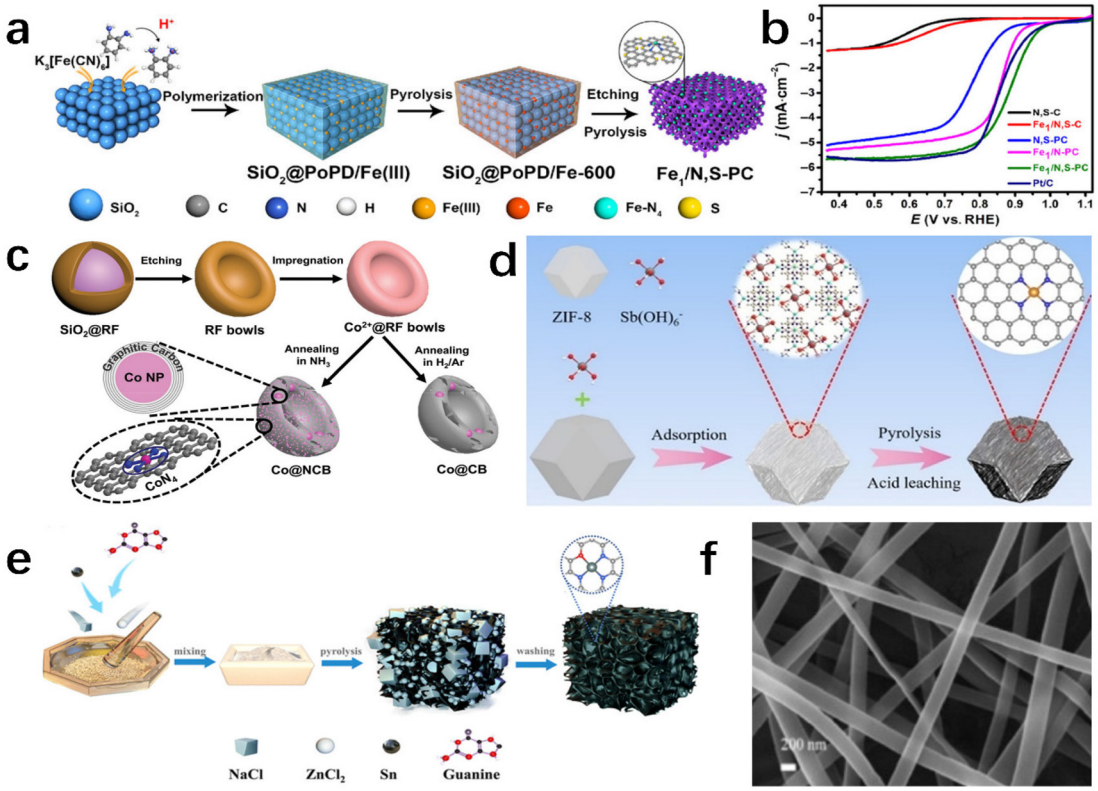

Fig. 3 (a and b) Schematic illustration of the formation and ORR polarization curves of Fe_1/N,S-PC. Reproduced with permission ref. 55. Copyright 2023, Tsinghua University Press. (c) Schematic illustration for the synthesis of Co@NCB. Reproduced with permission ref. 56. Copyright 2020, The Royal Society of Chemistry. (d) Illustration of the formation of a Sb SAC. Reproduced with permission ref. 57. Copyright 2021, Wiley-VCH. (e) Schematic illustration for the synthesis of a Sn SAC. Reproduced with permission ref. 58. Copyright 2023, Wiley-VCH. (f) SEM image of Fe_1-PAN-NFs. Reproduced with permission ref. 59. Copyright 2020, Elsevier.

addition, atomic layer deposition (ALD) designs and synthesizes fine catalysts at the atomic scale by accurately loading SAC onto the supports.[60,61] These studies have shown that the reasonable selection of synthesis methods is crucial for the preparation of catalysts.

2.2 Structural characteristics

Multiple atomic level characterization techniques have been used to explore the local structure of SACs.[62–64] Up to now, AC-HAADF-STEM was used to directly observe the metal active sites in catalysts. As the atomic number of the metal increases, the contrast in the image is greater and the spots are brighter.[65–67] Moreover, extended X-ray absorption fine structure (EXAFS) and X-ray absorption near-edge structure (XANES) can be used to characterize the electronic structure and coordination environment of the catalyst, such as the coordination type, coordination number, coordination distance, *etc*.[68,69] Other techniques have also been used to characterize the structure of SACs, such as X-ray powder diffraction (XRD), Mössbauer spectroscopy, *etc*.[70] The structure of SACs changes during the reaction, so precise *in situ* techniques are needed to observe the dynamic changes of the structure, such as *in situ* XAS. In general, all these excellent characterization techniques have played great roles in exploring the structure of SACs.

3. The impacts of atomic coordination

In addition to the synthesis strategy and structural characteristics, atomic coordination has a significant impact on the catalyst activity. For carbon-based SACs, the introduction of defects on carriers and coordination environment regulation can promote the ORR activity of the catalyst by influencing the electronic structure and geometric configuration. In this section, we focus on recent advances in the coordination environment and defect engineering.

3.1 The impacts of the coordination environment

Up to now, M–N–C catalysts have shown the best ORR performance. Therefore, the regulation of the coordination environment for the M–N–C is extremely important.[71,72] In most reported M–N–C catalysts, the metal atoms are coordinated as $M–N_4$. For example, Li *et al.*[73] synthesized ultrathin N-doped graphene mesh (SA Fe NGM) with $Fe–N_4$. Due to the ultra-thin 2D structure, the $Fe–N_4$ active sites were highly exposed, which also led to its excellent ORR performance with a half-wave potential of 0.83 V in 0.5 M H_2SO_4 solution. Similarly, Chen *et al.*[74] prepared nanosheets containing $Co–N_4$ active sites with excellent ORR activity using g-C_3N_4 as precursor (Fig. 4a). In addition, Yang *et al.*[75] also prepared CoTPyP catalysts with a

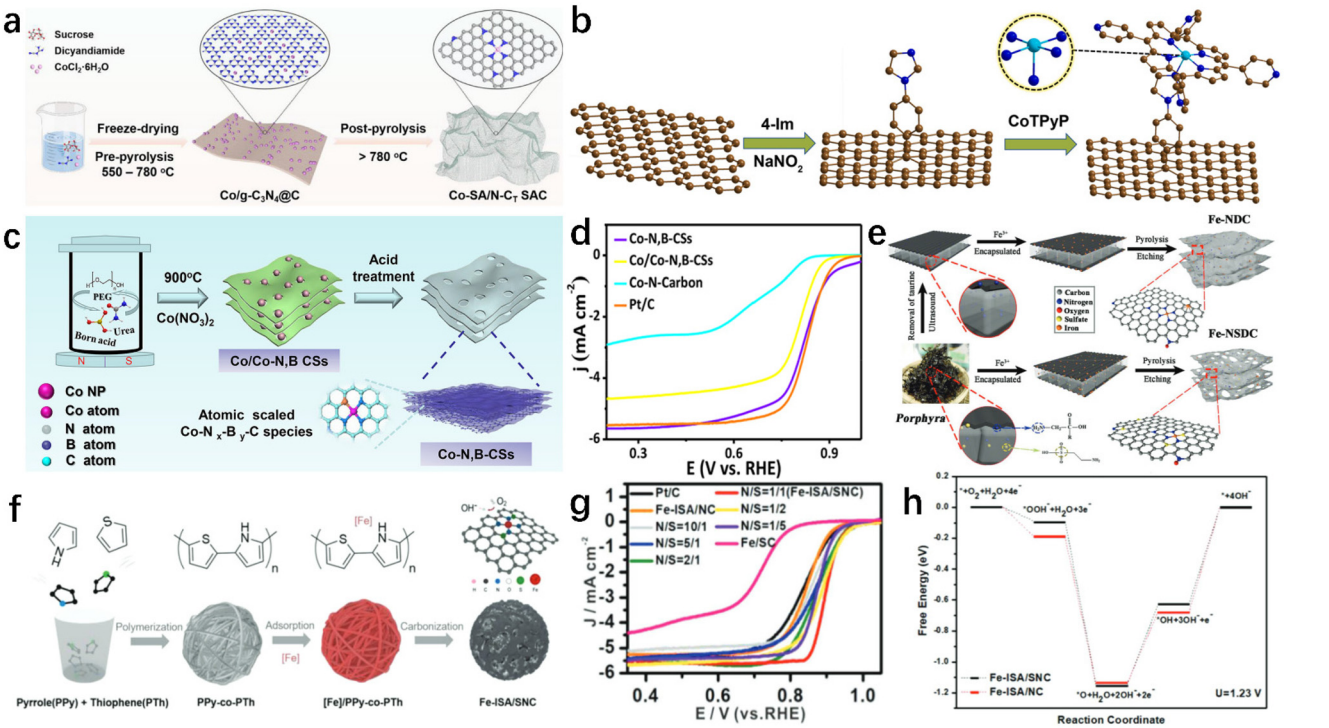

Fig. 4 (a) Schematic illustration of the synthetic procedure of Co-SA/N-C900. Reproduced with permission ref. 74. Copyright 2023, Elsevier. (b) Schematic illustrations of the synthesis of CoTPyP@Im-RGO. Reproduced with permission ref. 75. Copyright 2022, Elsevier. (c and d) Synthetic procedure and LSV curves of the Co–N,B-CSs. Reproduced with permission ref. 79. Copyright 2018, American Chemical Society. (e) Schematic illustration of the synthesis process for the Fe-NSDC. Reproduced with permission ref. 80. Copyright 2019, WILEY-VCH. (f–h) The synthetic process, ORR polarization curves and energy diagram of Fe-ISA/SNC. Reproduced with permission ref. 84. Copyright 2018, WILEY-VCH.

Co–N_5 structure (Fig. 4b). The electronic structure of the catalytic centre is mainly regulated by the liganded N and C atoms. However, during the development of SACs, more heteroatoms are used to regulate the coordination environment, such as S, P, B, O, Cl, *etc.*[76–78] In Fig. 4c, Guo *et al.*[79] prepared boron (B)-doped Co–N–C active sites confined in hierarchical porous carbon sheets (denoted as Co–N,B-CSs) using the soft template self-assembly pyrolysis method. The introduction of the element B provides electron-deficient sites and strengthens the interaction between the oxygen-containing intermediates and active sites. Therefore, the half-wave potential of Co–N,B-CSs is 0.83 V, which is similar to that of commercial Pt/C catalysts (Fig. 4d). In Fig. 4e, Zhang *et al.*[80] used a scalable $FeCl_3$-encapsulated porphyrin precursor pyrolysis strategy to obtain S-doped Fe–N–C catalysts. Characterization technologies verified that S doping produced excellent ORR activity by optimizing the charge and spin distribution of the Fe–N–C.

Interestingly, recent studies have shown that heteroatoms that are not directly coordinated to the metal active sites can also enhance the catalyst activity.[81–83] Although the heteroatoms are not directly attached to the metal active center, the heteroatoms doped in the carbon carrier will modulate the electronic structure of the active site by remote off-domain interaction, thus enhancing the ORR activity.[46] For example, Li *et al.*[84] designed a novel pyrrole-thiophene copolymer pyrolysis strategy to obtain Fe-ISA/SNC with S,N co-doping (Fig. 4f). By increasing the amount of S doping, the ORR performance of the Fe-ISA/SNC showed a volcano-shaped curve change. The $E_{1/2}$ of optimal Fe-ISA/SNC was 55 mV more positive than Pt/C (Fig. 4g). XAFS analysis and DFT calculations (Fig. 4h) showed that the introduction of S enriched the charge around the Fe–N active site, which facilitated the rate-limiting reductive release of OH* and ultimately promoted the ORR process. Similar results were obtained in the study of Chen *et al.*,[85] which demonstrated the positive effect of heteroatom doping on enhancing ORR activity.

3.2 The impacts of defect engineering

Defect engineering on carbon carriers can promote the anchoring of the central atoms, the rearrangement of the electron density, and also the exposure of more active sites. Therefore, defect engineering is equally indispensable for enhancing the catalytic activity of SACs.[86,87] The actual catalysts may contain a large number of defects, and it has been shown that appropriate defects enhance the ORR performance of the catalysts.[88] Yuan *et al.*[89] devised the decarboxylation-induced defect strategy for the preparation of defect-rich Co SACs. DFT calculations demonstrated that defects near the Co–N_4 active sites could substantially enhance the ORR activity by reducing the free energy of the intermediate OOH^-. The experiments of Wang *et al.*[90] also demonstrated that defects contribute to catalyst activity. In another study, Zong *et al.*[91] introduced defects on graphitic carbon nanospheres using KOH activation, resulting in Cu-SAs@N-CNS with a special Cu$(NC_2)_3$(NC) coordination configuration. DFT calculations showed that the formation of OOH* is the rate-limiting step in the four-electron process. Furthermore, the Cu$(NC_2)_3$(NC) had a low OOH* adsorption free energy (0.82 eV), which also confirmed the facilitating role of defects in the regulation of Cu-based single-atom catalysts. Later, Cui *et al.*[92] used a combined hydroxyl-functionalized and NH_4Cl-assisted etching strategy to obtain the CuN_4 sites with defective edges. The half-wave potential of 0.9 V confirmed the important influence of defects on the catalyst.

4. Carbon-based precious metal catalysts

Due to their unique ORR activity, precious metals have been the subject of intense research by numerous scientists The benefit of noble metal SACs is the maximum mass activity due to the maximum use of atoms. In this section, the study of noble metals in the ORR is presented.

4.1 Pt SACs

The platinum-based catalysts are currently the most active for ORR. Although Pt/C catalysts have been commercialized, their further advancement is hampered by negative reasons such as a lack of the Earth's platinum sources, a high price,[93,94] and poor catalytic stability.[95] Because of this, many scientists want to reduce the cost of Pt as much as possible and increase the cycling stability of the catalyst while ensuring high ORR activity. Common optimization schemes can be roughly divided into: increasing the density of Pt sites, modifying the coordination structure around the Pt, and doping heteroatoms. Next, we focus on the recent progress in enhancing carbon-based Pt SACs from these three aspects.

Li *et al.*[96] synthesized a Pt_1/NPC catalyst with isolated Pt atoms on N-doped porous carbon (Fig. 5a). The loading of platinum was 3.8 wt%, as measured by inductively coupled plasma photoemission spectroscopy (ICP-OES). In Fig. 5b, it also exhibited high activity on an ORR, with an $E_{1/2}$ = 0.887 V. Studies showed that this was attributed to the abundance of PtN_4 sites and the introduction of N atoms to enhance the electron transfer. Similarly, Liu *et al.*[97] reported a N-doped carbon Pt SAC (Pt_1–N/BP) for highly efficient $4e^-$ ORR. In contrast to Li *et al.*,[96] the Pt loading was only 0.4 wt%. The Pt_1/BP without N showed Pt agglomeration, suggesting that the introduction of N could help disperse the Pt atoms. Under acidic conditions, Pt_1–N/BP had a high ORR performance (Fig. 5c), but the Pt loading is lower, demonstrating its economical nature. The assembled H_2/O_2 fuel cell of Fig. 5d showed a power density of 680 mW cm^{-2}. More in-depth theoretical calculations using DFT showed that the adsorption of O_2 on g-P–N_1–Pt_1 was stronger than that of CO, verifying its CO tolerance. The free energy was also calculated in Fig. 5e and f, the ORR superpotential at the g-P–N_1–Pt_1 site was 1.74 V, and the desorption of OH was the rate-limiting step. At the g-P–N_1–Pt_1 position, the entire ORR process was much faster than at the g-P–N_1 position due to the small energy barrier of the preceding exothermic step and the rate-limiting step (*OH dis-

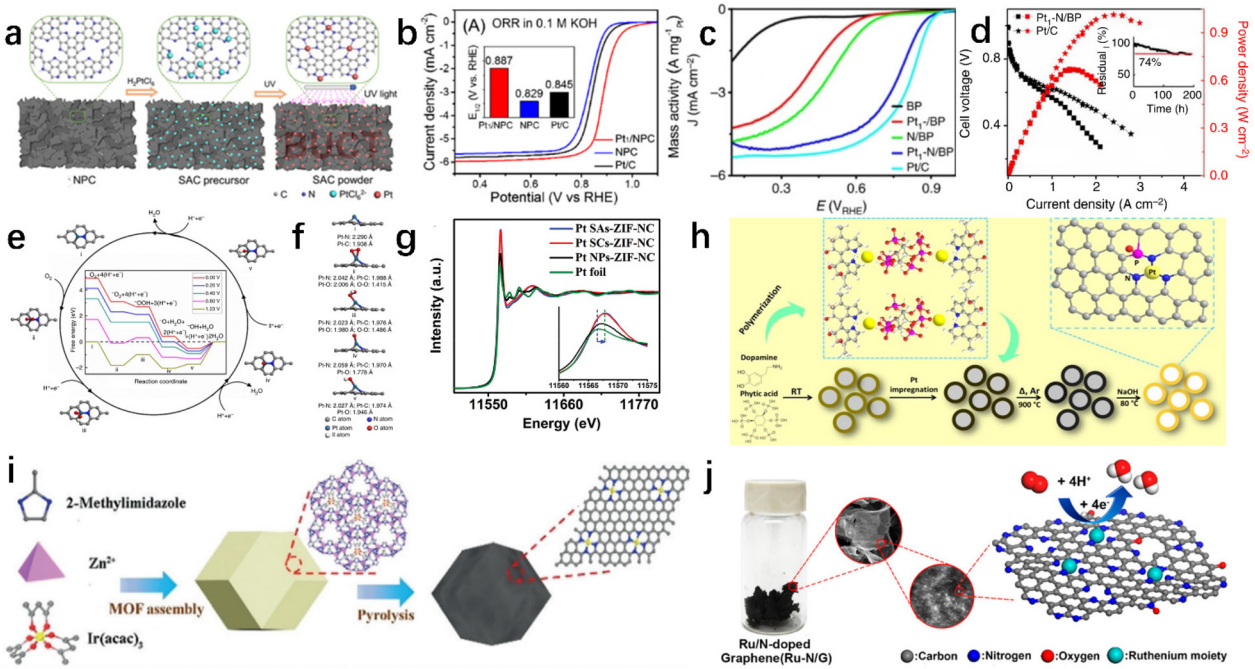

Fig. 5 (a and b) Schematic illustration, ORR polarization curves of Pt_1/NPC. Reproduced with permission ref. 96. Copyright 2018, American Chemical Society. (c–f) RRDE polarization curves, the voltages and power densities of H_2/O_2 fuel cells, the free energy diagram, side view, and bond lengths of Pt_1–N/BP. Reproduced with permission ref. 97. Copyright 2017, Nature. (g) The XANES spectra of Pt SAs–ZIF-NC. Reproduced with permission ref. 98. Copyright 2020, Wiley-VCH. (h) The preparation of the PtNPC. Reproduced with permission ref. 51. Copyright 2021, Wiley-VCH. (i) Schematic illustration of Ir/N–C. Reproduced with permission ref. 103. Copyright 2019, Wiley-VCH. (j) Illustration of Ru–N/G. Reproduced with permission ref. 105. Copyright 2017, American Chemical Society.

sociation). In another study, Song *et al.*[98] synthesized Pt SACs on the MOF-derived N-doped carbon. From the X-ray absorption near-edge structure (XANES) spectra in Fig. 5g, the platinum atoms were linked to N-electronegative atoms from the support, resulting in easier electron transfer from the Pt to the support, thereby increasing the 5d vacancy at the platinum sites. This was also the reason why Pt SAs-ZIF-NCs had the highest ORR performance. Furthermore, the adsorption of platinum atoms on pyrrolic N-containing ZIF-NCs was determined to be the most advantageous when compared with other forms of N (graphitic N, and oxidized N).

Inspired by N coordination, many scientists have placed heteroatoms into the Pt center, such as P and S, to alter the local coordination environment. Zhu *et al.*[99] synthesized PtNPC catalysts by introducing P (Fig. 5h). The optimization of the 5d orbitals, a left shift of the projected density of states (PDOS) of the 5d orbitals, and a deeper d-band center of PtN_3–PO, made it exhibit an excellent ORR performance. The NC, NPC and PtNC had poor ORR performance, but the PtNPC-0.5 had high ORR activity ($E_{1/2}$ = 0.85) with the introduction of P. Theoretical calculations showed the P atoms promoted the kinetics of the $4e^-$ route and prohibited the formation of peroxide species, further demonstrating that the P-coordinated Pt–N_3 sites were the active sites. It also showed the feasibility of the introduction of heteroatoms for enhancing ORR activity.

Chen *et al.*[100] loaded Pt onto S-doped graphitic carbon nitride (SGCN), and S-doping enabled the neighboring C and N atoms of Pt to be deficient in electrons, thereby enhancing the metal–support interaction. 20Pt/SGCN-550 had an ORR performance with $E_{1/2}$ = 0.91 V. DFT calculations showed that 20Pt/SGCN-550 had a lower d-band center than 20Pt/GCN, indicating that the binding of O-containing intermediates is weak, so the adsorption binding energy decreases. And the ΔG of 20Pt/GCN-550 to generate OH^- is also lower. Taken together, the introduction of S enhanced the interfacial interaction between the Pt and the carrier to enhance the ORR activity.

Pt can not only generate O_2 through the four-electron pathway of oxygen reduction but also generate H_2O_2 through the two-electron pathway. Theoretical studies suggested that two ORR pathways share a common intermediate of *OOH. So, in theory, the two-electron and four-electron processes can be selected by regulating the adsorption capacities of the catalyst and oxygen intermediates. Zhao *et al.*[101] successfully controlled the selectivity of the products by adjusting the coordinating heteroatoms around the Pt. The maximum hydrogen peroxide selectivity of Pt–S–C reaches 88%, which exceeded that of Pt–N–C (72.5%). The analysis of DFT calculations matched well with the experiment about H_2O_2 selectivity, indicating that adjusting the local coordination environment of the Pt can affect the intermediate the adsorption strength of the body determines the oxygen reduction pathway.

Therefore, for Pt-based SACs, there are significant differences in the performance depending on the Pt atomic coordination. Furthermore, coordination engineering of Pt-based SACs can efficiently adjust the $2e^-$ or $4e^-$ process of ORR to meet our urgent needs.

4.2 Other precious metal SACs

In addition to Pt SACs, other noble metal SACs also exhibited both high ORR activity and stability.[102] In a recent study, Xiao *et al.*[103] synthesised Ir-SAC with a half-wave potential of 0.864 V in acidic conditions. It exhibited a record-high TOF of 24.3 per e per site per s, which is 5.6 times higher than commercial Pt/C, demonstrating the strong ORR application potential of Ir noble metals (Fig. 5i). In another study, Cui *et al.*[104] synthesized Ru-SAS@N-ACSS by anchoring Ru single atoms on the pore edge of activated carbon spheres by a simple sol–gel sealing method. Theoretical calculations showed that the $Ru–N_4$ on the edge had a lower binding energy of ORR intermediates compared with the $Ru–N_4$ on the carbon plane, leading to its superior ORR activity. Moreover, in Fig. 5j Zhang *et al.*[105] synthesized Ru–N/G with acidic ORR activity by anchoring single Ru atoms on graphene oxide. In addition to these, Kim *et al.*[106] explored the performance of Pd SACs in the production of H_2O_2. All of these discoveries provided a way for the development of noble metal-based ORR SACs.

5. Carbon-based transition metal catalysts

Due to their unique electronic structures and relatively low prices, transition metals have received much attention and many ORR catalysts with outstanding performance have been successfully synthesized. Numerous investigations have shown that adding transition metals (Fe, Co, Ni, and Cu, *etc.*) to nitrogen-doped carbon is an efficient way to increase ORR activity.[107–113] For the carbon-based transition metal catalysts, it is obvious that the transition metal is essential to the functioning of the active center, but the exact active center remains undetermined and controversial, and the $M–N_x$ component is the active site for catalytic ORR, according to the more widely accepted theory. In addition the differences caused by the inherent nature of the coordination engineering of the N and C atoms controls the electrical structure of the catalytic core more so than the metal atoms themselves. Different coordination numbers and different configurations of the central atoms lead to changes in the electronic structure and thus exhibit different catalytic activities.[114] The latest research on transition metal-doped carbon electrocatalysts (especially Co, Fe, Cu, and Ni elements) will be summarized and discussed below. Table 1 summarizes the active site structures of some excellent carbon-based transition metal SACs and their performance in ORR.

5.1 Fe SACs

In 1964, Jasinski *et al.*[121] pioneered the use of cobalt phthalocyanines in ORR reactions in alkaline conditions, thus initiating the study of $M–N_4$ macrocyclic organics for ORR reactions. The Fe- and N-doped carbon (Fe–N/C) materials are now the most researched transition metal ORR catalysts due to their extraordinarily high ORR activity and four-electron selectivity, making them the most promising alternative to commercial Pt/C catalysts.

ZIFs are assembled from transition metal ions and imidazole rings *via* tetrahedral coordination, and they can uniformly pre-arrange with metal–N_4 linkages within an ordered 3D support.[122,123] Many ZIFs not only exhibit excellent thermal and chemical stability, but also contain an abundant source of nitrogen in the imidazole ligand, and after pyrolysis, the ZIF is converted into regular nitrogen-doped carbon carriers.[124] Inspired by ancient overhang-eave architectures, Hou *et al.*[125] designed and synthesized overhang-eave structures containing isolated Fe atoms using silica as a medium (Fe/OES, Fig. 6a), which can provide more extended edges as three-phase exchange points (Fig. 6b), not only accelerating the mass transport of the ORR but also maximizing the exposure of the atomically dispersed/catalytically sites. As shown in Fig. 6c, Fe/OES exhibited excellent ORR activity with $E_{1/2}$ = 0.85 V. As shown in Fig. 6d, for $Fe–N_4–C$, step (ii) and step (v) required an external force to overcome the activation energy barrier, and step (v) is considered the rate-determining step (RDS) of the ORR reaction. Step (i) required a substantially higher endothermic energy for $V_{Fe}–N_4–C$ (V_{Fe} symbolizes Fe vacancy) as the contrastive sites, which was the RDS of ORR. The above shows that

Table 1 Summary of carbon-based SACs for electrocatalytic reduction of ORR

Catalyst	Active site	E_{onset} (V *vs.* RHE)	$E_{1/2}$ (V *vs.* RHE)	Stability	Ref.
Fe SAC/N–C	FeN_5	—	0.890	Only minute differences after 5k CV cycles	115
Fe-SAs–N/C-20	Edge-hosted FeN_4	—	0.915	A negligible negative shift after 10k successive cycles	116
FeN_4–O–NCR	FeN_4–O	1.050	0.942	Only a 5 mV degradation in $E_{1/2}$ after 5000 CV cycles	77
Fe–N/P–C	$Fe–N_3P$	0.941	0.867	A negligible negative shift for 36 000 s	78
CoN_4/NG	CoN_4	0.980	0.870	A high relative current of 92% after scanning 36 000 s	117
Co SAs/N–C(900)	CoN_2C_2	—	0.881	No obvious decay in $E_{1/2}$ after 5000 continuous potential cycles	118
Ni SAs–NCs	NiN_x	—	0.850	After continuous working for 20 h, the current retention rate is still more than 90%	119
Cu-SA/N–C	CuN_4	0.990	0.895	No significant reduction in $E_{1/2}$ was observed after 5000 continuous potential cycles	120

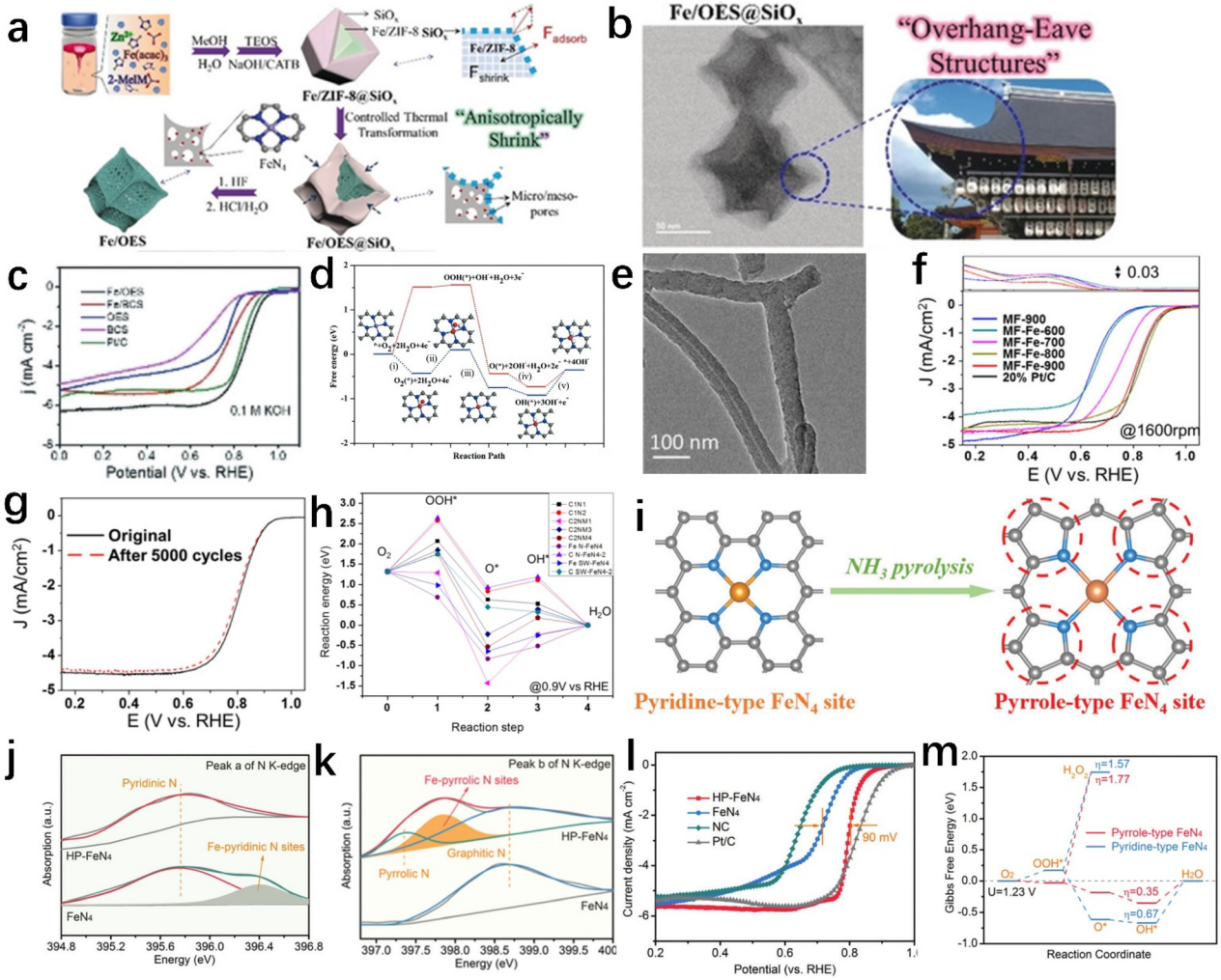

Fig. 6 (a–d) Synthesis process, STEM images, LSV curves, and ORR free-energy paths of Fe/OES. Reproduced with permission ref. 119. Copyright 2020, Wiley-VCH Verlag GmbH & Co. KGaA, Weinheim. (e–h) TEM images, RRDE voltammograms, the durability tests, and free energy diagram of MF-Fe-800. Reproduced with permission ref. 120. Copyright 2017, American Chemical Society. (i) Preparation process of a high-purity pyrrole-type FeN_4 structure. (j and k) Deconvoluted features of peak a and peak b of the N K-edge spectra. (l and m) ORR polarization curves and free energy diagram of HP-FeN_4. Reproduced with permission ref. 123. Copyright 2020, Royal Society of Chemistry.

Fe–N_4–C sites do participate in the ORR reaction as active sites. Similar conclusions were also reached by the work of Lu *et al.*,[126] when they prepared Fe and N co-doped porous carbon nanotubules (MF–Fe-*T*, *T* stands for pyrolysis temperature, Fig. 6e). Electrochemical tests showed that the Fe,N-doped nanotubes synthesized by the same method were more electrocatalytically active for ORR than the N-doped nanotubes alone, implying that Fe–N_4 promoted the association of oxygen species. The catalyst prepared at 800 °C is the most effective in the series, with E_{onset} = 0.98 V (Fig. 6f). The MF–Fe-*T* catalyst also exhibited good durability: in Fig. 6g there was only a 7 mV decrease in $E_{1/2}$ after 5000 cycles. As can be seen in Fig. 6h, steps (3) or (4) for FeN_4-doped graphene can be recognized as the RDS, denoting an advantageous binding with oxygen species. Stone–Wales Fe–N_4 activates the neighboring C atom so that it also contributes to the ORR reaction. From the experiment and theory, the FeN_4 sites played the important role in ORR activity.

Among the M–N–C SACs, the usual nitrogen species are pyridinic, pyrrolic, and graphitic N. Among them, pyridinic N is the most common, but recent experiments and theoretical calculations have shown that pyrrolic N is more ORR-catalytic active.[127–129] For example in Fig. 6i, high-purity pyrrole-type FeN_4 sites (HP-FeN_4) were successfully prepared by Zhang *et al.*[129] Soft X-ray absorption spectroscopy (sXAS) proofed Fe–N sites of HP-FeN_4 were confirmed to be high purity as pyrrole-type coordination (Fig. 6j and k). In Fig. 6l, HP-FeN_4 exhibited a higher E_{onset} than FeN_4 and a more positive $E_{1/2}$ than FeN_4. According to DFT calculations, the charge distribution of pyrrole-type FeN_4 and pyridine-type FeN_4 was noticeably different, and the iron's valence state was more positive. In the free energy diagram in Fig. 6m, pyrrole-type FeN_4 was preferable for ORR because of the lower Gibbs free energy differences between O_2 and OOH*. Furthermore, in a $4e^-$ route, pyrrole-type FeN_4 had a lower thermodynamic overpotential

(0.35 eV) than pyridine-type (0.67 eV). In particular, on the pyrrole-type FeN_4 structure, the reduction of OOH* to H_2O_2 is 0.2 eV higher compared with the pyridine-type FeN_4 structure (1.77 eV *vs.* 1.57 eV), indicating that the $2e^-$ reduction pathway is largely inhibited. Overall, pyrrole-type FeN_4 would be the ideal sites for ORR because of the lower limiting potential and is more conducive to $4e^-$ reactions.

However, the intermediates have an excessively high adsorption energy on the FeN_4 sites and this affects their desorption to participate in the subsequent reactions, so this does not show the best activity.[130,131] In addition to the Fe–N_4 structure, the researchers found that FeN_2 also has excellent ORR performance and conducted in-depth research on this because of the receding of the adsorption energy of the intermediates. Shen *et al.*[132] introduced a number of dispersed FeN_2 sites on the N-doped carbon. Efficient ORR catalysts (FeN_2/NOMC) with iron atoms dispersed on the framework surface can be obtained by the subsequent removal of SBA-15 and agglomerated Fe-based particles with HF etching, leaving only the FeN_2 sites (Fig. 7a). As shown in Fig. 7b, the FeN_2/NOMC exhibit superior activity with an $E_{1/2}$ of 0.863 V. The extended X-ray absorption fine structure (EXAFS) data analysis of Fig. 7c showed the coordination number of N is 2.0, and FeN_2/NOMC-3 exhibits an almost total absence of Fe–Fe and Fe–C bonds, indicating that the majority of the Fe atoms are scattered as mononuclear particles in the FeN_2 fraction. The DFT in Fig. 7d indicates that the overpotential of FeN_2 is reduced by 0.12 V compared with FeN_4, and the reduced interaction with $*O_2$ and *OH intermediates is the cause of the increased ORR activity. And the existence of FeN_2 sites was more beneficial for enhanced electron transport. The same idea was also obtained in the experiments of Song *et al.*[133] They successfully synthesized iron-based ORR catalysts containing multiple active sites. The DFT calculations and tests showed that the following active sites on Fe–N_x/C catalysts for ORR have a structure–activity relationship: Fe–N_2C > Fe–N_4C > Fe_4–NC > N–C > Fe_4–C > C. These calculations provide theoretical support for subsequent studies of Fe coordination engineering.

Recently, Lin *et al.*[115] first introduced metal ions into UiO (bpdc) with pyrolysis and acid leaching. Fe SAC/N–C catalysts with FeN_5 sites were obtained. The $E_{1/2}$ of Fe SAC/N–C was 0.89 V (Fig. 7e). DFT calculations were performed to completely comprehend the superb ORR activity that the FeN_5 site exhibited. Three models in Fig. 7g, Fe-4pN, Fe-4pN-OH, and Fe-4pN-py, were investigated in depth. In Fig. 7h, for the ideal Fe-4pN model, all the reaction steps are thermodynamically favorable, but in practice, the ideal Fe-p4N is converted to Fe-p4N-OH due to abundant OH^-. For Fe-4pN-OH, the formation of *OOH is the RDS. The energy barrier of Fe-p4N-py would be lowered to 0.11 eV if the extra OH group were replaced with pyridine. Although the whole reaction process was still limited by the formation of *OOH, the catalytic activity of Fe atoms coordinated to five pyridine nitrogen atoms for ORR is very considerable. And in a study, the five-coordinated Fe–N_x configuration prepared by Lai *et al.*[134] exhibited better ORR activity in

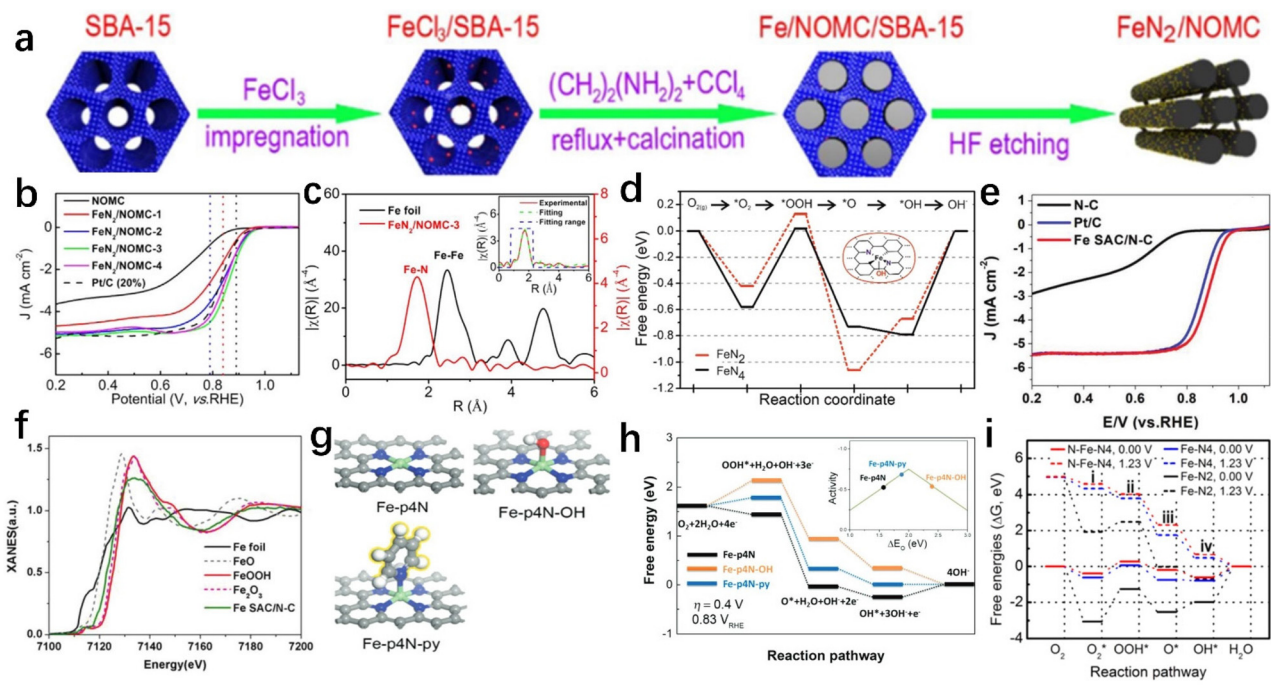

Fig. 7 (a–d) The synthetic procedure, ORR polarization, EXAFS spectra, and free energy diagram for FeN_2/NOMC. Reproduced with permission ref. 126. Copyright 2017, Elsevier. (e–h) LSV curves, XANES spectra, three models with various coordination environments, and free energy diagrams of Fe SAC/N–C. Reproduced with permission ref. 128. Copyright 2019, Wiley-VCH. (i) Free energy diagrams of the N–Fe–N_4, Fe–N_4, and Fe–N_2 in acid media. Reproduced with permission ref. 129. Copyright 2017, American Chemical Society.

acidic media compared with the lower-coordinated Fe–N_x configuration. Three theoretical models, N–Fe–N_4, Fe–N_4, and Fe–N_2, were constructed to explain the reasons in Fig. 7i. For N–Fe–N_4, and Fe–N_4, the free energies of all the successive intermediate steps at 0 V are reduced compared with Fe–N_2, but the N–Fe–N_4 structure showed the lowest energy barrier, indicating that the O_2 molecules were more easily reduced to H_2O completely on the N–Fe–N_4 structure. In addition, when the OH* adsorption energy was compared, the N–Fe–N_4 structure's OH adsorption energy was 2.88 eV, which was much lower than the adsorption energies of Fe–N_4 and Fe–N_2. The lower hydroxyl adsorption energy protects the active center from deactivation. The above indicates that even if the coordination mode is the same, different synthesis methods, carbon carriers, and defect richnesses can affect the actual performance of the catalyst. Therefore, research on catalysts should not only focus on the theory.

Defective Fe active sites have been extensively studied. For example, Jiang *et al.*[116] prepared catalysts with Fe–N_4 sites anchored on 3D layered porous carbon (Fe-SAs–N/C-20, Fig. 8a and b). Fe-SAs–N/C-20 exhibited excellent ORR performance with a half-wave potential of 0.915 V, in Fig. 8c. ^{13}C solid state nuclear magnetic resonance (ssNMR) showed that the integrated intensity ratios of sp^3- to sp^2-hybridized carbons (I_{sp^3}/I_{sp^2}) grew with defect increases, indicating that defects make it easier for C–N bonds to break. Six possible conformations of Fe–N_4–C were calculated by DFT. As shown in Fig. 8e, the least overall reaction free energy change is shown in the defective Fe–N4-6r-c2 near the gap's edge, suggesting that selective CN bond cleavage (SBC) can adjust the coordination environment of pyridine N. In another study, Xiao *et al.*[135] incorporated FeN_4 edge sites into graphene (Fe/N–G-SAC) by a new self-sacrificing template method (Fig. 8f). This method used an extremely excess amount of Fe precursors, and the Fe clusters not only promoted the formation of graphitized structures but also promoted the generation of FeN_4 partially near the Fe clusters. After etching the Fe clusters, edge-enriched FeN_4 sites were obtained. Due to these structural properties, the Fe/N–G-SAC had excellent activity and stability. The assembled zinc vacancy cells also exhibit excellent performance. It was calculated by DFT that the closer the distance between the Fe cluster and the Fe–N_4 part, the lower the relative formation energy (E_f). Therefore, the introduction of excessive Fe clusters during the synthesis process made it easier to form the Fe cluster/Fe–N_4-1 structure. This eventually leads to the formation of edge-dominated FeN_4 sites in the sample after the Fe clusters are removed (Fig. 8g). The conformational differences between the edge site and the in-place site were compared. Due to the decrease in the number of N coordinations, a significant charge redistribution occurs at the Fe–N_4 edge sites, allowing a more favorable electron transfer from the Fe atom to the neighboring N atom, and the higher Bader charge

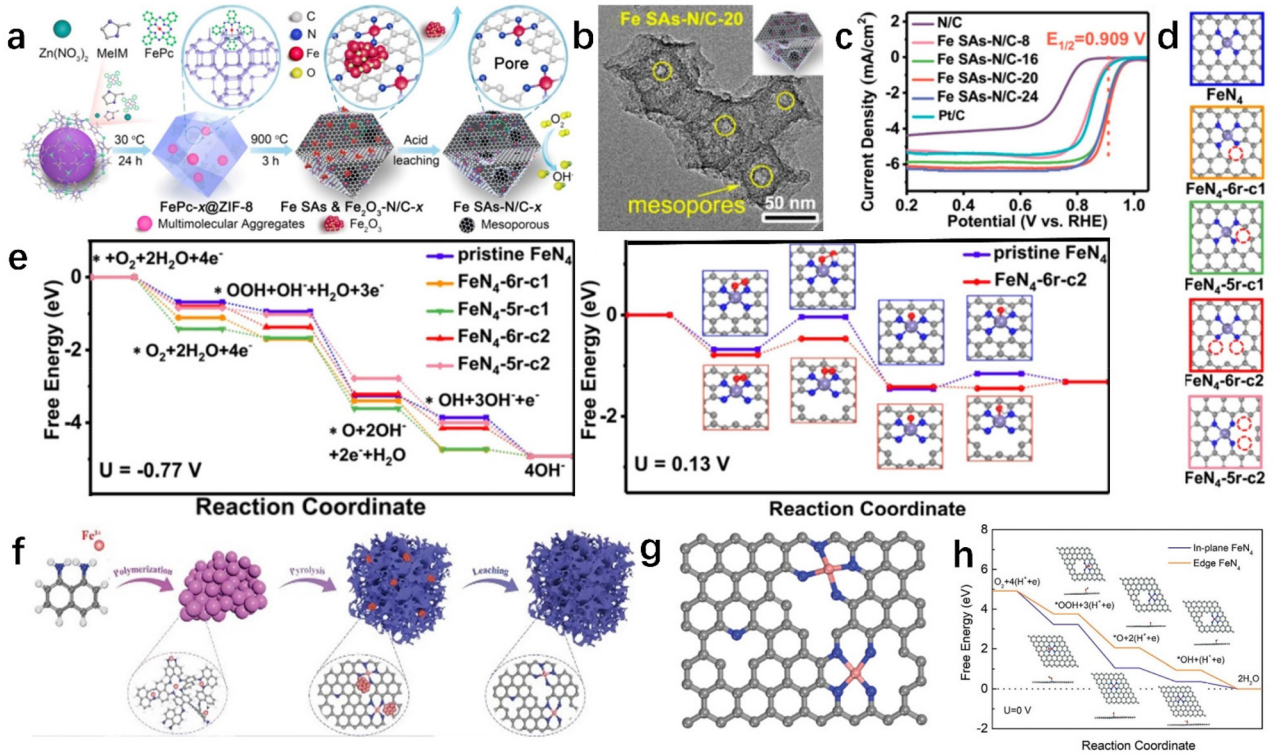

Fig. 8 (a–e) Schematic illustration, HRTEM, LSV curves, five possible atomic configurations, and free energy diagram of Fe-SAs–N/C. Reproduced with permission ref. 130. Copyright 2018, American Chemical Society. (f–h) Scheme of synthesis, structure, and free energy diagrams of Fe/N–G-SAC. Reproduced with permission ref. 131. Copyright 2020, Wiley-VCH.

estimated also demonstrates this. The partial density of states (DOS) of the Fe calculation showed that with the negative shift of the d-band center on the edge FeN_4 site, the binding strength of the adsorbates on the edge site is also relatively diminished. The RDSs on the in-plane Fe–N_4 sites were known to be the OH desorption; however, after a thorough investigation, it was shown that the adsorption free energy of OH* (G_{OH*}) on the edge site was larger, indicating a faster OH desorption process that was beneficial for the ORR (Fig. 8h). Similar conduct had also been observed by Chen *et al.*[136] The sur-FeN_4-HPC catalyst they synthesized using the edge effect also has excellent ORR activity.

The introduction of other heteroatoms will also significantly enhance the ORR activity of the catalyst. For example, Mun *et al.*[137] doped S functionalities into the carbon plane to modulate t-doped S functionalities into the carbon plane to modulate the electron-absorbing/electron-giving properties of the Fe–N_4 sites (Fig. 9a). X-ray photoelectron spectroscopy (XPS), shown in Fig. 9b, indicated that the S existed in both thiophene-like S (C–S–C) and oxidized S (C–SO_x) forms. The C–S–C enriched the carbon plane with electrons, thus enhancing the adsorption of the ORR intermediate on Fe–N_4, while the introduction of C–SO_x reduces the Fe d-band center. Interestingly, similar trends were seen in the $E_{1/2}$ of the FeNC–S–MSUFC catalysts with regard to the ratios of oxidized S and thiophene-like S (Fig. 9c), demonstrating that the kind of S affected the ORR activity of the Fe–N_4.

In another study combining experimental and theoretical, Peng *et al.*[77] synthesized FeN_4–O–NCR in which the Fe–N_4 sites were modulated by Fe–O bonds (Fig. 9d). As shown in Fig. 9e, FeN_4–O–NCR had good ORR activity due to its special coordination structure. DFT calculations similarly demonstrated that FeN_4–O–NCR was beneficial for the ORR process. When simple axial O ligands are present, this led to a weaker binding of FeN_4/C and FeN_4/NC to *OH, thereby improving the ORR performance. A later study from Gong *et al.*[138] in Fig. 9f also introduced O into FeN_4, forming Fe(Zn)–N–C catalysts with Fe@O@Fe bridge bonds. Compared with the single-atom FeN_4 site, the O bridge-bonded Fe sites have 10 times higher activity in terms of turnover frequency (TOF, 3.2 per es per sites *vs.*

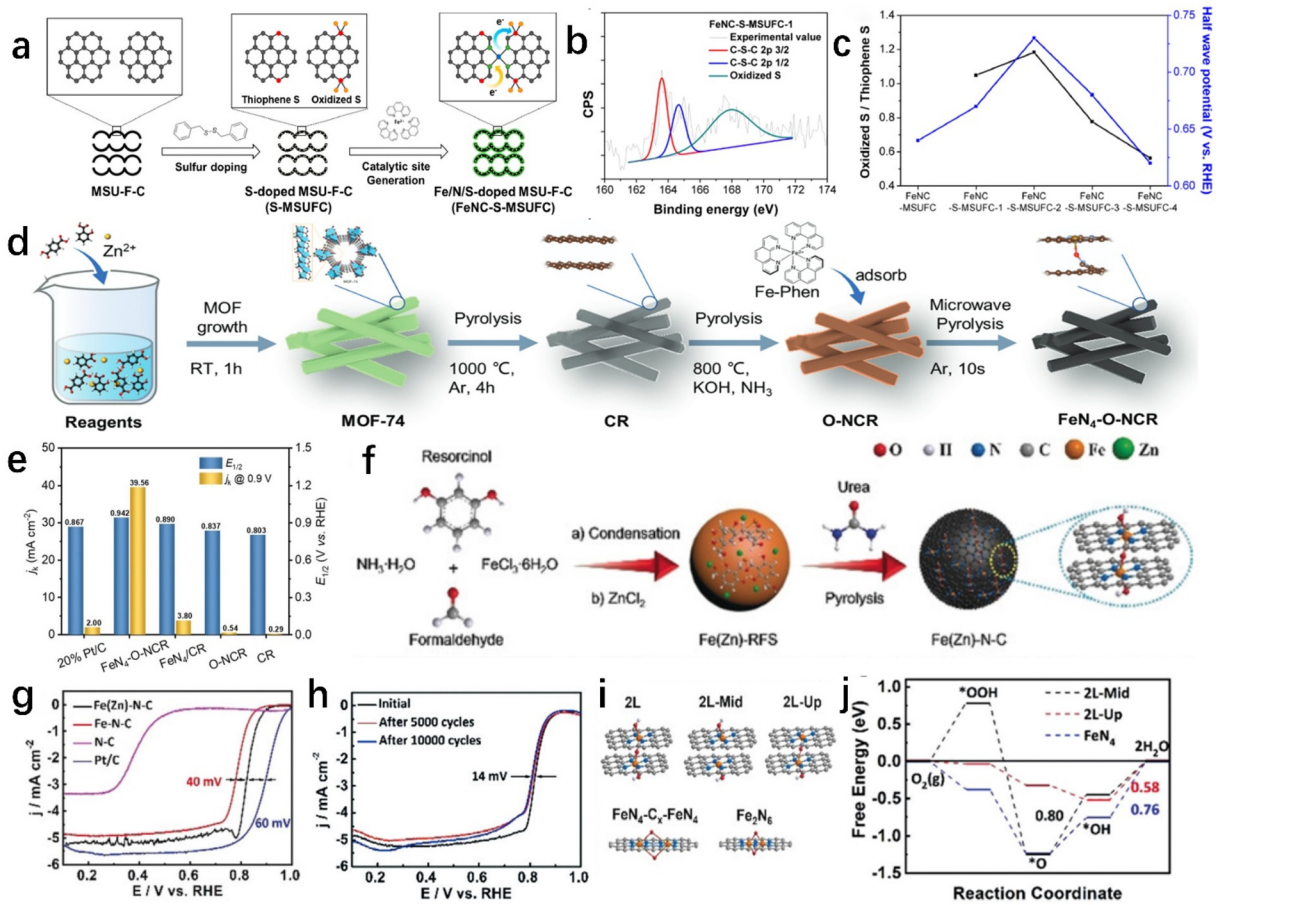

Fig. 9 (a and b) Schematic representation of the synthesis and S 2p XPS spectra of FeNC–S–MSUFC. (c) Relationship between the ratio of oxidized S and thiophene-like S and ORR activity. Reproduced with permission ref. 133. Copyright 2019, American Chemical Society. (d and e) Scheme of the synthesis, $E_{1/2}$ and j_k of the FeN_4–O–NCR. Reproduced with permission ref. 77. Copyright 2022, Wiley-VCH. (f–i) Synthesis, LSV curves, the durability tests, and illustration of proposed various structures of Fe(Zn)–N–C. (j) Gibbs free energy diagrams at 1.23 V on FeN_4, 2L-Mid, and 2L-Up sites. Reproduced with permission ref. 134. Copyright 2020, Wiley-VCH.

0.32 per es per sites) and have promising half-wave potential (0.83 V), in Fig. 9g. Meanwhile, after 10 000 continuous cycles, the $E_{1/2}$ reduced only by 14 mV (Fig. 9h). Gibbs free energies were calculated in Fig. 9i for the three models (2L-Mid, 2L-Up, and FeN_4). As shown in Fig. 9j, 2L-Up had the lowest overpotential and the final *OH dissociation step was the only heat-absorption process, suggesting a facilitative effect of the indicated bridge-bonded O on the improvement of catalytic activity. The electron flow from the Fe d orbital to O was found using Bader charge analysis, resulting in a weaker adsorption of the remaining d electrons on O_2 and ultimately excellent ORR performance. A later study from Yuan *et al.*[78] showed that the introduction of P heteroatoms was beneficial for the adsorption/desorption of oxygen intermediates, boosting the catalytic ORR performance. Three N atoms and one P-anchored Fe ($Fe–N_3P$) were found to make up the compound Fe–N/P–C. It can be inferred from a comparison of the free energy distributions of $Fe–N_4$ and $Fe–N_3P$ that the O_2 molecule caught by the Fe atom went along a downward trajectory. However, the fact that $Fe–N_3P$'s free energies were lower than those of Fe–N4 suggests that the O_2 molecules can easily adsorb and form a strong bond on $Fe–N_3P$ active sites.

5.2 Co SACs

Despite having outstanding characteristics, Fe–N–C electrocatalysts are usually affected by Fenton reactions:[139] the intermediates generated in the center of the Fe sites contain large amounts of active oxygen, which corroded the carbon matrix and rapidly reduce its activity, leading to the destruction of the electrocatalyst.[140] Co is another commonly used transition metal, also with good activity and stability but without initiated Fenton reactions. Compared with other cobalt-based catalysts, cobalt-based SACs have received a lot of attention because of their improved durability, more flexible synthesis strategy, and readily tunable coordination environment for the active Co sites.[139] Similar to FePc, CoPc has been studied by many scientists for its good ORR activity. As early as 1990, Vasudevan *et al.*[141] published a summary of the relevant factors affecting CoPc. For CoPc/C, the ORR activity and stability were significantly increased after pyrolysis at 700 °C. However, with continued rising temperature above 800 °C the macrocyclic structure was damaged, which had an impact on the activity. These suggested that the structure of the central metal atom has a strong influence on activity; as demonstrated by the experiment of Yuasa *et al.*,[142] the Co–N–C catalyst was pyrolyzed at 700 °C to give a dense pyrrole-type $Co–N_4$ coordination. Continued warming to 1000 °C resulted in a large accumulation of metallic Co and reduced activity. In summary, the $Co–N_4$ fraction is indeed the dominant activity, and the appropriate pyrolysis temperature is critical for the formation of active site sites.

To date, the study of $Co–N_x$ coordination configurations can be widely divided into two categories: experimental and theoretical. Although Co–N–C has a variety of coordination modes, CoN_4 is the most commonly used model.[143,144] Zhang *et al.*[145] investigated in depth the CoN_4–graphene catalysts with pyridine-N and pyrrole-N coordination by DFT calculations (Fig. 10a and b). Despite both CoN_4–G having ORR activity, the specific catalytic mechanisms are different. The CoN_4–G(A) catalysts exhibited higher activity, whereas the CoN_4–G(B) catalyst, owing to the high response barrier of H_2O_2 formation (1.07 eV), exhibited higher 4-electron selectivity (CoN4–G(A) and CoN4–G(B) are the names given to the Co atoms coordinated by four pyridinic-N atoms and four pyrrolic-N atoms, respectively). In an earlier study, Yang *et al.*[117] prepared the single-atom Co–N–C catalysts with atomically dispersed CoN_4 (denoted as CoN_4/NG, Fig. 10c). In Fig. 10d and e, XANES and EXAFS analyses showed that one Co atom in CoN_4/NG was coordinated to four surrounding nitrogen atoms, forming a CoN_4 group, which was the main reason for its excellent ORR performance. As shown in Fig. 10f, Wang *et al.*[146] further designed a locally distorted CoN_4 conformation, where the charge can be transferred more rapidly from the Co atom to the N due to the disruption of the symmetric electron distribution. Compared with plane CoN_4, it showed a lower energy barrier for the RDS and thus had a better ORR performance (Fig. 10g). In addition, the free energy diagrams of locally distorted $Co–N_3C_1$ and $Co–N_2C_2$ structures were also calculated in Fig. 10h. The RDS of $Co–N_3C_1$ and $Co–N_2C_2$ is the reduction of OH*, where the ΔG_{max} values are 0.43 eV for $Co–N_3C_1$ and 0.54 eV for $Co–N_2C_2$, suggesting that $Co–N_3C_1$ has higher ORR activity. For a more comprehensive summary comparison, four types of Co–N contribution categorised as CoN_x (x = 1–4) were estimated by Sun *et al.*,[147] in Fig. 10i. The CoN_4 profiled most nearly resembles the optimum free-energy pathways. The overpotential was further calculated and found to increase in the order of $CoN_4 < CoN_3 < CoN_2 < CoN_1$, indicating that CoN_4 has better catalytic performance (Fig. 10i).[147]

In a theoretical study, a computational study of the ORR mechanism of $Co–N_4$ electrocatalysts with pyridine-N coordination by Kattel *et al.*[148] had verified again the significant effect caused by different N coordinations on the $Co–N_4$ activity. Compared with graphitic CoN_2 defects, graphitic CoN_4 defects were energetically favorable and had better stability. Therefore, CoN_4 should be the more promising catalytic center (Fig. 10j and k). Due to the defective configuration of $Co–N_4$ with pyrrole-N coordination and the O_2 bound in an end-pair configuration, it is more inclined to produce H_2O_2 than the $Co–N_4$ with pyrrole-N coordination. As shown in Fig. 10l, the adsorption of OOH^- on CoN_4 was weak, and a second catalytically active center was required to further reduce H_2O_2, which is also consistent with the experimental results.[118,149,150] The $4e^-$ reaction without OOH^- intermediate generation occurred in the CoN_2 part, which is similar to the catalytic process at the $Fe–N_2$ site.[151] The later work of Sun *et al.*[152] also drew similar conclusions.

Another study from Yin *et al.*[118] found that $Co–N_2$ species interacted more strongly with peroxides than $Co–N_4$ and promoted the four-electron reduction process of ORR (Fig. 11a). Experiments also demonstrate that $Co–N_2$ sites can exhibit superior ORR performance. By regulating the pyrolysis temperature, Co SAs/N–C(800) with CoN_4 sites and Co SAs/N–C(900)

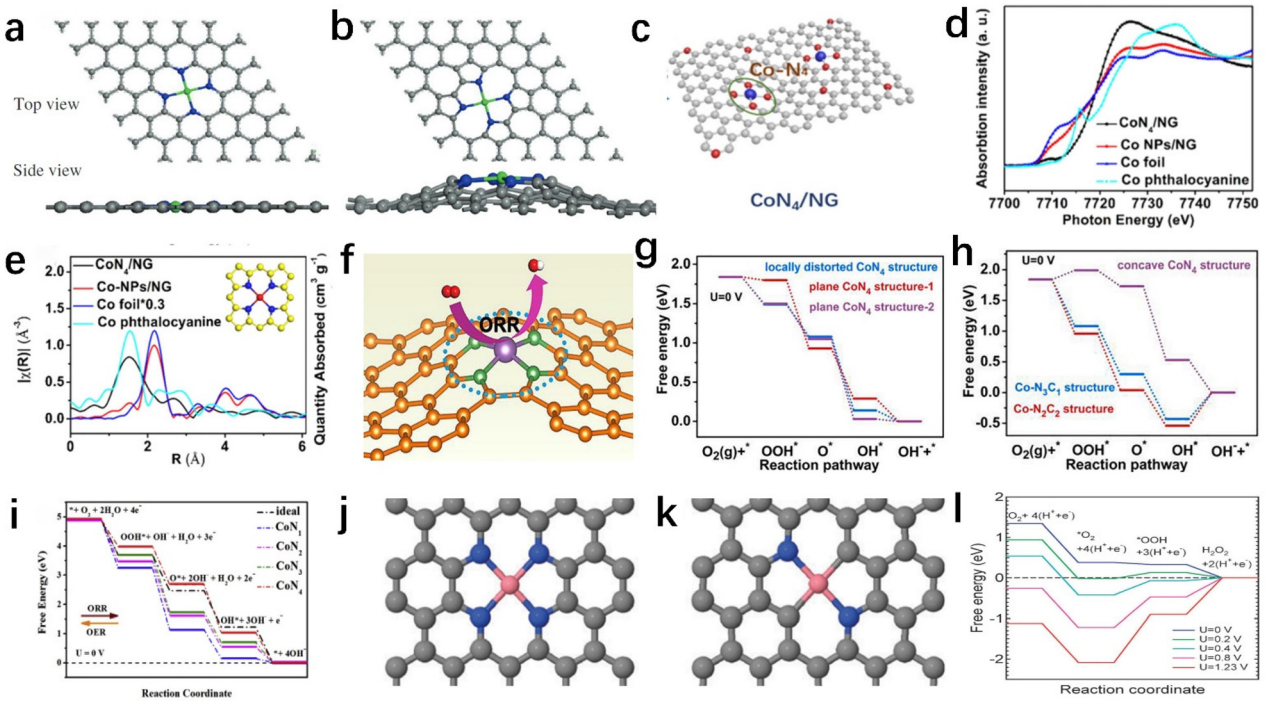

Fig. 10 (a and b) Top and side views of the optimized structures of CoN_4–G(A) and CoN_4–G(B). Reproduced with permission ref. 141. Copyright 2020, Wiley-VCH. (c–e) Schematic illustration, XANES Co K-edge spectra, and Fourier-transforms of Co K-edge spectra for CoN_4/NG. Reproduced with permission ref. 142. Copyright 2018, Elsevier. (f) Distorted Co–N_4 structure. (g) Free energy diagram on different structures of CoN_4. (h) Free energy diagram for the ORR on CoN_2C_2 and CoN_3C_1. Reproduced with permission ref. 143. Copyright 2022, Elsevier. (i) Free-energy diagrams for the ORR and OER pathways on CoN_x (x = 1–4). Reproduced with permission ref. 144. Copyright 2019, Elsevier. (j and k) Schematic illustration of CoN_4 and CoN_2. (l) Free-energy diagram for the reduction of O_2 to H_2O_2 on the CoN_4 defect. Reproduced with permission ref. 145. Copyright 2019, Royal Soc Chemistry.

with CoN_2C_2 sites were obtained. In Fig. 11b, the ORR activity of Co SAs/N–C(900) was better than Co SAs/N–C(800).

Zhang *et al.*[153] performed DFT calculations on the detailed kinetic and thermodynamic behavior of the ORR on three different CoN_2–G models (Fig. 11c–e). Similar to the conclusions obtained by Kattel *et al.*[148] all three CoN_2–G models favored the ORR response, but with subtle differences. The catalyst with the highest levels of catalytic activity and four-electron selectivity is CoN2–G(A). In contrast, the two-electron pathway is favored due to the weak adsorption energy of the H_2O_2 generated on CoN_2–G(B) (−0.39 eV) which is easily desorbed.

Similar to Fe–N–C catalysts, doping with nonmetallic heteroatoms (B, P, S, *etc.*) also enhances the Co–N–C ORR performance by tuning the electronic properties of neighboring carbon atoms.[154,155] For example, Liu *et al.*[156] anchored Co single atoms to ultrathin N- and P-doped porous carbon nanosheets to obtain CoSA/NPC catalysts (Fig. 11f). DFT were carried out to theoretically comprehend the ORR reaction mechanism in order to understand the impacts brought about by P doping. As shown in Fig. 11g, the RDS of Co/N_3P is smaller than that of Co/N_4 (0.445 eV *vs.* 0.466 eV) and the charge distribution at the Co active site is unbalanced due to P doping (Fig. 11h), which is beneficial for the adsorption of oxygen species. As a result, the ORR catalytic activity of Co/N_3P is better compared with CoN_4 ($E_{1/2}$ = 0.87 V).

In another study by Xu *et al.*,[157] B was introduced into Co–N–C to obtain Co–NBG (Fig. 11i), and this sample exhibited excellent ORR performance. In Fig. 11j, the $E_{1/2}$ of Co–NBG was 0.792 V. The effect of B doping on the ORR catalytic activity of Co–gN_4 based on DFT was investigated by Fu *et al.*[158] Because the electronegativity of B is lower than C, when graphite was doped with B, an area close to Co–gN_4 developed that was positively charged, requiring the Co sites to lose additional electrons in order to achieve equilibrium. Additionally, the adsorption of Co sites to intermediates was less as the B concentration increased, which increased the reactivity. In addition to B and P, Zhang *et al.*[76] synthesized Co single atoms on the porous N,S-co-doped carbon (Co-SAs/NSC, Fig. 11k). The coordination states of the S atoms at the single atom core were shown to be crucial in lowering the reaction barrier, which increased the ORR kinetics, according to DFT calculations. Therefore, the ORR activity of the catalyst can be optimized by adjusting the electronic structure of the catalyst by selecting different electronegativity heteroatoms.

It was also found that co-doped graphene with two or more heteroatoms would be more electrocatalytically active due to synergistic effects compared with single heteroatom-doped graphene.[159–161] As shown in Fig. 11l, Xu *et al.*[162] obtained CoPS@SPNC through carbonization of ZIF-67 followed by a simultaneous sulfidation and phosphatization. The introduc-

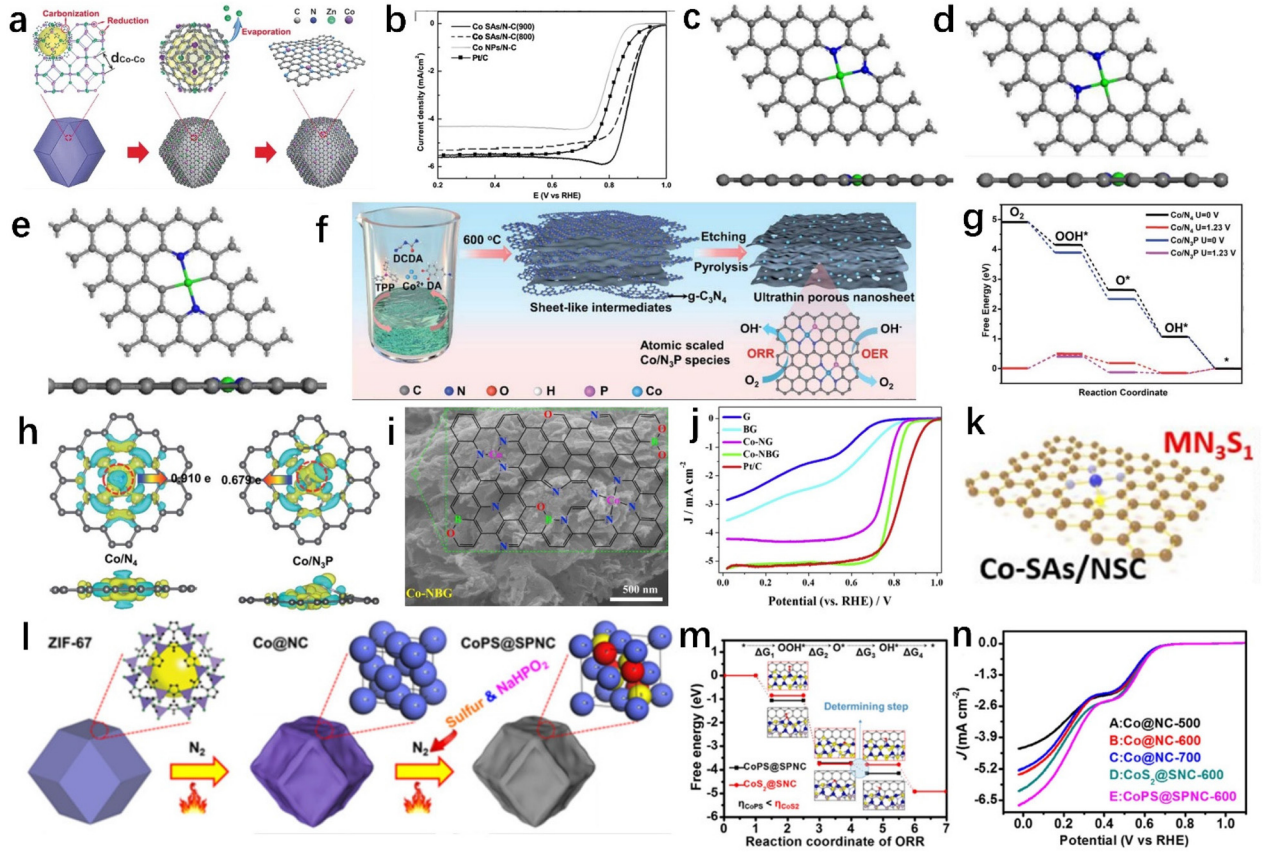

Fig. 11 (a and b) The formation and RRDE polarization curves of Co SAs/N–C. Reproduced with permission ref. 148. Copyright 2016, Wiley-VCH. (c–e) Top and side views of three structures of CoN2–G. Reproduced with permission ref. 151. Copyright 2017, The Electrochemical Society. (f) Scheme of synthesis of the CoSA/NPC. (g and h) The Gibbs free energy diagram, charge density differences and Bader charge analysis of Co/N_4 and Co/N_3P. Reproduced with permission ref. 154. Copyright 2021, Royal Society of Chemistry. (i and j) SEM image and schematic illustration, and RRDE polarization curves of Co–NBG. Reproduced with permission ref. 155. Copyright 2019, Elsevier. (k) Schematic illustration of single-atom Co-SAs/NSC. Reproduced with permission ref. 76. Copyright 2019, American Chemical Society. (l–n) Scheme of synthesis, free energy diagram, and ORR polarization curves of CoPS@SPNC. Reproduced with permission ref. 160. Copyright 2022, Elsevier.

tion of heteroatoms decreased the overpotential of the ORR to enhance the catalytic activity, as calculated by DFT (Fig. 11m), which is consistent with the experimental results (Fig. 11n).

In addition to the $4e^-$ ORR discussed above, Co SAC was found to have the best performance in the production of H_2O_2 among the transition metal SACs. As shown in Fig. 12a, Jung *et al.*[163] found that ΔG_{OOH^*} could be adjusted by attaching a functional group to the $Co–N_4$ molecule ΔG_{OOH^*}. G_{OOH^*} rises from 3.9 eV to 4.1 eV when electron-rich species, such as O*, are adsorbed close to the $Co–N_4$ molecule ($Co–N_4(O)$), approaching the ideal value for the formation of H_2O_2. It showed that the $2e^-$ ORR produced H_2O_2 with a high degree of selectivity when O* was present near the Co atom. Therefore, they synthesized $Co_1–NG(O)$ for the electrochemical production of H_2O_2 in Fig. 12b. Using the Koutecky–Levich equation, the kinetic current density for H_2O_2 production from $Co_1–NG(O)$ is 2.8 ± 0.2 mA cm^{-2} at 0.65 V (Fig. 12c). Similarly, Li *et al.*[164] conducted a mechanistic study of the synthesized Co–POC–O for H_2O_2 production. As shown in Fig. 12d, they found that the high H_2O_2 production rate was due to the synergistic effect of the $Co–N_x–C$ and OfG sites responsible for ORR reactivity and two-electron selectivity, respectively. More recently, Shen *et al.*[165] compared in detail the catalytic activity and selectivity for the H_2O_2 production of five-coordinated O–$Co–N_2C_2$ and $Co–N_4$ by DFT calculations, in Fig. 12e and f. The ΔG_{OOH^*} of Co in O–$Co–N_2C_2$ (Fig. 12g) was closer to 4.2 eV than that of CoN_4. Beyond this, at the equilibrium potential for H_2O_2 production, the RDS energy on O–$Co–N_2C_2$ was much lower than that on $Co–N_4$, indicating that the penta-coordinated O–$Co–N_2C_2$ was inherently more active and selective than traditional tetra-coordinated $Co–N_4$ for the generation of H_2O_2 (Fig. 12h).

In general, the optimization of Co-based catalysts was similar to that of Fe-based catalysts. The coordination structure of the Co–N–C part can be modified and controlled by adjusting the coordination number of the N, and the non-metallic heteroatom doping can also enhance the ORR activity by adjusting the electronic structure to the central Co atom. Different from the Fe-based catalysts, Co-based catalysts can be used for the production of H_2O_2 due to the inherent properties of the Co metal.

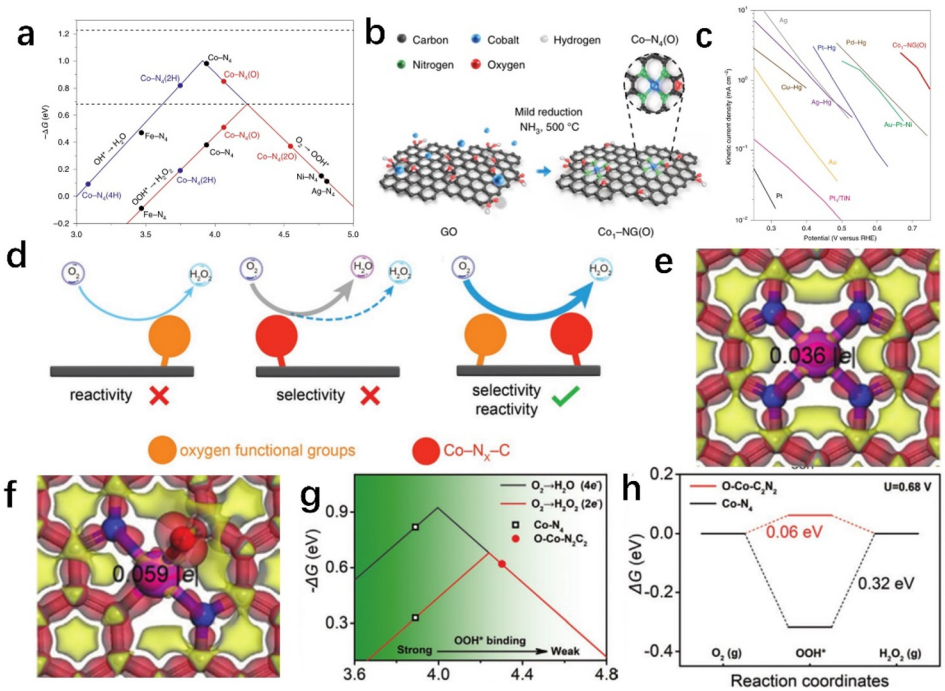

Fig. 12 (a) Calculated catalytic activity volcanoes. (b) Scheme of synthesis of Co_1–NG(O) SAC. (c) Summary of H_2O_2 production activity. Reproduced with permission ref. 161. Copyright 2020, Nature. (d) Schematic illustration of atomic Co–N_x–C sites and oxygen functional groups for H_2O_2. Reproduced with permission ref. 162. Copyright 2019, Wiley-VCH. (e–h) Deformation densities, calculated catalytic activity volcanoes, and calculated reaction energetics of the 2e$^-$ ORR of O–Co–N_2C_2 and Co–N_4. Reproduced with permission ref. 163. Copyright 2022, Wiley-VCH.

5.3 Ni SACs

Ni metal is also commonly used in the 4e$^-$ ORR reaction, but the NiN_4 site is hindered from its further development due to its weak oxygen-binding capacity.[166] However, it is possible to reduce the energy barrier between the Ni-based center and oxygen intermediates by precisely regulating the coordination environment of Ni–N–C, thereby improving the oxygen reduction performance.[167]

Jiang *et al.*[119] synthesized nitrogen-doped carbon sheets (Ni SAs–NCs) with dispersed Ni atoms by pyrolysis (Fig. 13a). Ni SAs–NCs have good ORR activity with an $E_{1/2}$ of 0.85 V (Fig. 13b). In addition, the stability of Ni SAs–NC is excellent; after continuous working for 20 h, the current retention rate was still more than 90%. Its high activity was thought to be due to the transition of O_2 to O* intermediates facilitated by the Ni–N_x center.[168] Qiu *et al.*[169] in-depth investigated the four-electron ORR catalytic performance of N,Ni-co-doped graphene in alkaline conditions by DFT calculations. O_2 reacts at the active sites and is successively converted to oxygenated intermediates OOH*, O*, and OH*, eventually producing water. For this catalyst, the rate-limiting step is the generation of OOH* intermediates, the adsorption energy of OOH* on N, Ni-co-doped graphene was higher than that on N single-doped graphene and Ni-doped graphene, and the O–O bond was longer in N,Ni-co-doped graphene. The above constitute the reasons for the high ORR activity of Ni–N–C. In addition, compared with pure graphene, doping N on graphene promotes the anchoring of Ni, which enhanced the ORR activity by increasing the density of Ni active sites.

In a theoretical study, Liang *et al.*[170] established 15 different Ni–N–C coordinated doped graphene systems using nitrogen-doped graphene as a carrier, and comprehensively and theoretically studied the important effect of the coordination environment of Ni-based catalysts on ORR activity. As shown in Fig. 13c, the adsorption capacity of tetracoordinate Ni–N–C-gra for oxygenated intermediates was weak, while the adsorption capacity and η^{ORR} increased with the decrease of N doping amount. In contrast, three-coordination Ni–N–C-gra highly adsorbed intermediates showed that OOH* rapidly dissociates and that there was an excess amount of OH* being adsorbed (Fig. 13d). In addition, it was also found that on the Ni–N–C sites modified with OH functional groups, the adsorption strength of the intermediate product was reduced, thereby enhancing the ORR activity. The η^{ORR} of $Ni(OH)N_3$ was even lower than for Pt (0.42 V *vs.* 0.45 V). In summary, these theoretical studies have provided a solid theoretical basis for future research on Ni-based ORR catalysts.

5.4 Cu SACs

Cu has been extensively studied for its excellent ORR activity. In an earlier study, Thorum *et al.*[171] reported a simple method for the adsorption of insoluble copper complexes onto carbon black. The generated [Cu(Hdatrz)] complex had high ORR activity with E_{onset} = 0.86 V. However, the stability of the syn-

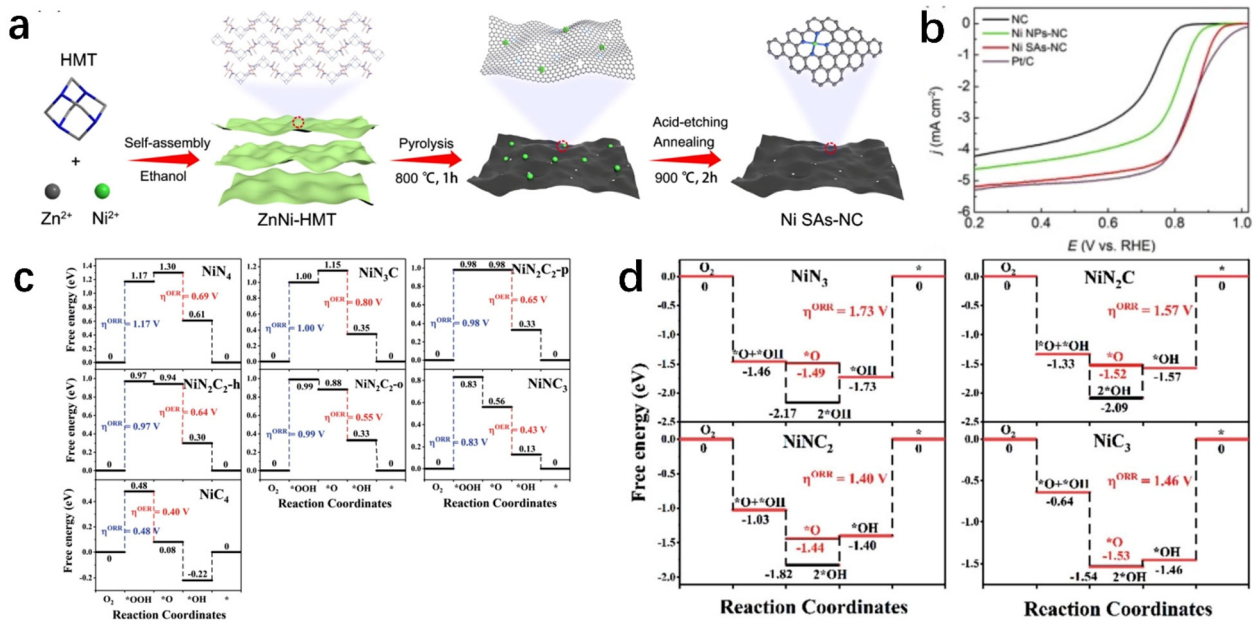

Fig. 13 (a and b) Scheme of synthesis and LSV curve of Ni SAs–NC. Reproduced with permission ref. 166. Copyright 2022, Elsevier. (c and d) Free energy diagrams for the ORR and OER on four-coordinated and on three-coordinated Ni–N–C-gra. Reproduced with permission ref. 169. Copyright 2020, Royal Society of Chemistry.

thesized complex is very poor and cannot be used in practice. So far, the introduction of Cu metal into the carbon skeleton by pyrolysis was an important method commonly used to improve the stability of samples. Qu *et al.*[120] generated atomically dispersed Cu-SA/N–C catalysts by a simple gas migration strategy (Fig. 14a). The valence state of Cu in Cu-SA/N–C was between Cu(0) and Cu(ii) as shown by XPS in Fig. 14b and EXAFS in Fig. 14c. Due to its highly dispersed CuN_4 active center, the $E_{1/2}$ of Cu-SA/N–C was 0.895 V (Fig. 14d). Xiao *et al.*[172] calculated the reaction mechanisms and thermodynamic pathways of the fundamental reaction steps involved in ORR on CuN_4 active sites by DFT. The calculations showed that this coordination structure had a higher performance in catalytic ORR compared with conventional metals, indicating that CuN_4 co-doped graphene is an effective catalyst for ORR. More recently, Ma *et al.*[173] controlled the generation of CuN_3 sites by increasing the pyrolysis temperature (900 °C, Fig. 14e). The electrochemical test indicated that atomically dispersed Cu catalysts with $Cu–N_3$ moieties had better ORR performance than Cu–N–C catalysts with $Cu–N_4$ sites. The DFT theoretical calculations were consistent with the experimental results. For both CuN_4 and CuN_3 (Fig. 14f and g), O_2 adsorption was the RDS for oxygen reduction, and the O_2 adsorption upslope for CuN_3 (0.17 eV) was much weaker than that of CuN_4 (0.87 eV), explaining the high activity of CuN_3 (Fig. 14h and i).

The chemical valence state of the central Cu atom also plays a significant role in enhancing the ORR activity of Cu-based ORR catalysts. Sun *et al.*[174] prepared a series of Cu-based ORR catalysts (Cu-SA/NC(*meso*)) with different ratios of Cu^{1+} and Cu^{2+} using ammonia as the reducing agent (Fig. 15a). Testing found that ORR activity increased with the addition of Cu^{1+} sites. The Cu^{1+}-SA/NC(*meso*)-7 achieved excellent ORR activity with $E_{1/2}$ = 0.898 V (Fig. 15b) and J_k = 5.36 mA cm^{-2} (Fig. 15c). As shown in Fig. 15d, DFT calculations indicated that the energy required for the rate-limiting step of Cu^{1+}-SA is 0.46 eV, which is lower than that of Cu^{2+}-SA (0.71 eV). Moreover, the Cu single catalysts rich in Cu^{1+} sites had good binding energies with OOH adsorption in the ORR process, resulting in high electrocatalytic activity in alkaline media. From the DFT calculations, it can be concluded that the coordination state of the S atom plays an important role for the monoatomic centre in lowering the reaction potential barrier and facilitating the onset of ORR kinetics. The study of the CuN_2C_2 site by Han *et al.*[175] also demonstrated the presence of high ORR activity. They simulated three different CuN_2C_2 models. Although the geometries are different, the potential determining step is the same, which is the protonation of $*O_2$ to *OOH. The calculations revealed that more negative charges were transferred to $*O_2$ on Cu/CNT-8 due to the different substrate structures of the three models. In addition, the maximum structural deformation occurred when O_2 was adsorbed on Cu/CNT-8, which was also considered to be the reason for its high activity. Therefore, it was very comprehensive to correlate the metal valence state of the central site with the coordination mode to study the reason for its high activity towards ORR.

Wu *et al.*[176] synthesized N-doped graphene (Cu–N©C) with Cu(I)–N active sites by pyrolysis of ligand-saturated copper phthalocyanines. XPS showed that most of the Cu is present in the form of Cu^+. As shown in Fig. 15e, the results of EXAFS showed that the number for the Cu–N©C-60 coordination was about 2 and Cu was present as CuN_2 sites. Interestingly, treat-

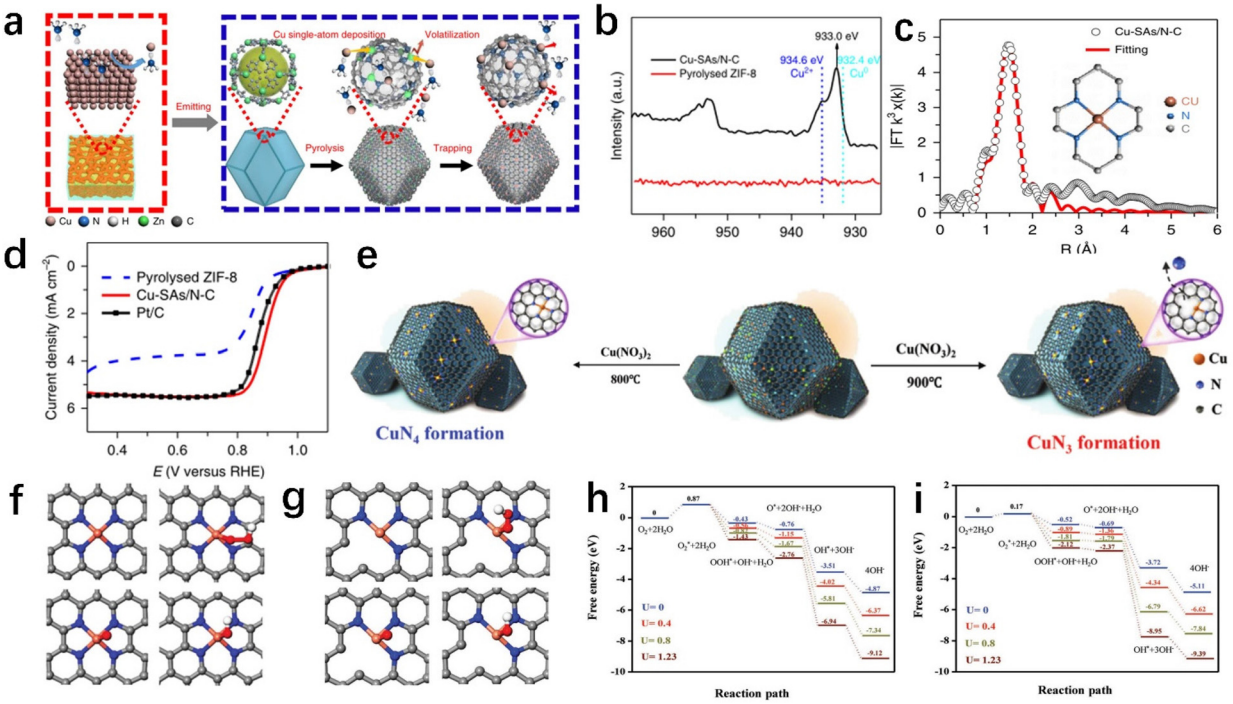

Fig. 14 (a–d) Scheme of synthesis, copper 2p XPS spectra, EXAFS fitting curve, and RRDE polarization curves of Cu-SAs/N–C. Reproduced with permission ref. 171. Copyright 2018, Springer Nature. (e) Scheme of synthesis of CuN_3 and CuN_4. (f and g) View of the model of the CuN_4 model and CuN_3 model. (h and i) Free energy diagrams for the ORR process on CuN_4 and CuN_3 at different overpotentials. Reproduced with permission ref. 173. Copyright 2020, Wiley-VCH.

ment of Cu–N©C-60 with HNO_3 solution resulted in a significant reduction in ORR activity after conversion of some of the Cu(I) sites to Cu(II) sites, indicating that Cu(I)–N(CuN_2) was the active site for catalytic ORR (Fig. 15f). As shown in Fig. 15g, Bader charge analyses showed that the Cu valence states in the CuN_2 and CuN_4 fractions are closer to Cu_3N (Cu(I)) bulk and CuPc (Cu(II)). The top of the volcano plot was Cu–N_2, indicating that the Cu–N_2 sites were the active sites (Fig. 15h).

The high ORR activity of CuN_2 was also demonstrated by Li *et al.*[177] It was well known that the adsorption energy of O_2 and OOH* on the active sites and the elongation of the O–O bonds had a decisive influence on oxygen reduction.[32,178,179] They investigated in depth the chemisorption capacity between O_2 and Cu–N_2. It showed that Cu–N_2 had a suitable O_2 adsorption energy and that long O–O distances were readily available on Cu–N_2, making it easier for O_2 to be activated. Xie *et al.*[180] also compared the adsorption preferences of O_2 on $Cu^I@N_2$, $Cu^{II}@N_4$, and C atoms: $Cu^I@N_2$ > C atoms > $Cu^{II}@N_4$. As a result, the ORR kinetics of Cu–N–C catalysts with $Cu^I@N_2$ and $Cu^{II}@N_4$ fractions were different. While Cu^{II} cannot directly engage in the ORR process, Cu^I may, and the Cu–N–C bond contains a C atom that is implicated in oxygen reduction. The ORR activity of Cu–N–C was therefore mainly derived from $Cu^I@N_2$, which was also in general agreement with the findings of Wu *et al.*[176]

In addition to this, scientists have also investigated other CuN_x conformations. Hu *et al.*[181] synthesized a N-doped carbon support (CuN_{2+2}/C) with CuN_{2+2} sites (Fig. 15i). DFT theoretical calculations showed that, in Fig. 15j, the changed electronic structure of Cu and the resultant orbital overlap caused by proper symmetry with the degenerate π* orbital of the adsorbed oxygen molecule allow the CuN_{2+2} sites to enable O_2 activation. The PDOS of the Cu_1 3d orbital showed that the d-band center ɛd of CuN_{2+2} was higher than that of CuN_4, indicating that the Cu–O bonding on CuN_{2+2} is tighter. Also, the protonation barrier for PDS on CuN_{2+2} was lower. Therefore, CuN_{2+2}/C had excellent ORR activity. As shown in Fig. 15k, CuN_{2+2}/C had a more favorable half-wave potential.

Coordination with other non-metallic heteroatoms also resulted in stronger ORR activity of the Cu active center. In Fig. 15l, Shang *et al.*[182] synthesized S–Cu-ISA/SNC with an unsymmetrically coordinated Cu–S_1N_3 moiety. S–Cu-ISA/SNC reflected a half-wave potential of 0.918 V (Fig. 15m). The Cu K-edge *in situ* XANES spectra for S–Cu-ISA/SNC were further investigated, and the edge position was gradually relocated to the lower energy, along with a reduction in the intensity of the white line, illuminating the significance of Cu valence alterations in ORR reaction (Fig. 15n). As shown in the volcano-type plot (Fig. 15o), the Cu atom in Cu–S_1N_3 had the best ORR activity, which was consistent with the experimental results.

5.5 Other transition metal SACs

Other metals have also been attempted for electrocatalytic ORR reactions, such as Zn, Cr, Mn, Mo, W, *etc*. For example, Li

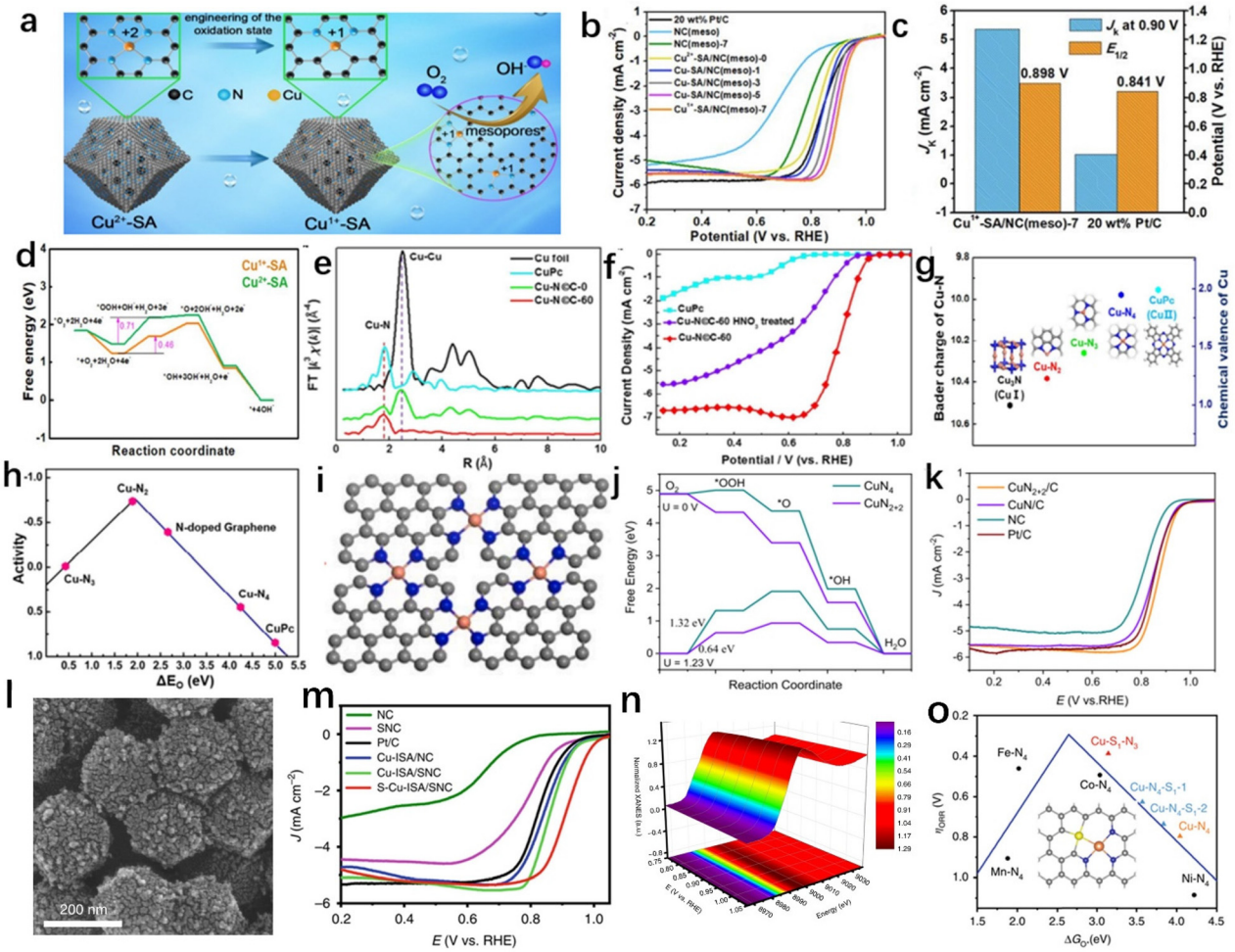

Fig. 15 (a–d) Schematic diagram, LSV curves, the comparison of J_k and $E_{1/2}$, and the free energy diagram of Cu-SA/NC(*meso*). (e–h) Fourier-transformed EXAFS spectra, ORR polarization curves, Bader charge and corresponding chemical valence, volcano plot between ORR activity and ΔE_0 for Cu–N©C-60. Reproduced with permission ref. 174. Copyright 2016, Royal Society of Chemistry. (i–k) Schematic diagram, free energy diagrams, and LSV curves of CuN_{2+2}/C. Reproduced with permission ref. 181. Copyright 2022, Elsevier. (l–o) SEM image, polarization curves, Cu K-edge XANES spectra, and ORR overpotential volcano plot of S–Cu-ISA/SNC. Reproduced with permission ref. 182. Copyright 2020, Nature.

et al.[183] synthesized Zn–N–C catalysts with Zn–N_x active sites by slowly heating poly(*o*-phenylenediamine) and $ZnCl_2$ at 1 °C min^{-1} (Fig. 16a). Due to the strict control of temperature, the atom loading of Zn in Zn–N–C is as high as 9.33 wt%. As shown in Fig. 16b, the $E_{1/2}$ of Zn–N–C in alkaline conditions was up to 0.873 V. It showed that, compared with Fe–N_4, Zn–N_4 had weaker binding to OH* and weaker corrosion of the active center, so Zn–N–C has better corrosion resistance and stability (Fig. 16c). Chen *et al.*[184] synthesized N-doped graphene with dispersed W–N_x (x = 3, 4, 5) sites by adjusting the parameters of pyrolysis atmosphere, temperature, and time, in Fig. 16d. The W–N–C catalyst with W–N_5 sites exhibited a high ORR activity with an E_{onset} of 1.01 V and $E_{1/2}$ of 0.88 V (Fig. 16e). Moreover, the WN_5 catalyst also had good ORR activity in 0.1 M $HClO_4$. As shown in Fig. 16f, the strong ORR activity of the W metal was attributed to the appropriate interaction of OH^- with the metal according to DFT calculations, which agreed with the experimental findings.

Mn SACs are also popular for ORR.[185] Lin *et al.*[186] prepared a Mn SAC (Mn-SA) with Mn-pyridinic-N_4 sites with an $E_{1/2}$ of 0.870 V. Comparing the three models of Mn–N_x (x = 1, 2, 3), it has been discovered that the RDS of Mn-pyridinic-N_4 only had an energy uphill of 0.3 V at η = 0.4 V, indicating that the reason for the high ORR activity is the appropriate adsorption of intermediates. Shang *et al.*[187] designed a carbon-based Mn–N_2C_2 electrocatalyst (Fig. 17a). In 0.1 M KOH, the $E_{1/2}$ of this catalyst is 0.915 V (Fig. 17b). Four types of Mn active center with different N coordination numbers were constructed. DFT calculations showed that MnN_2C_2 was stable and the whole ORR process was exothermic, indicating a better ORR performance for Mn–N_2C_2 (Fig. 17c). In another study, by Shang *et al.*[188] (Fig. 17d), the S-modified MnSAs/S-NC catalysts had high half-wave potentials ($E_{1/2}$ = 0.916 V). The high ORR activity of MnSAs/S-NC was discovered to be the product of an electronic and atomic synergistic interaction between the Mn and the co-modified S,N carbon carrier. Mn-based catalysts containing

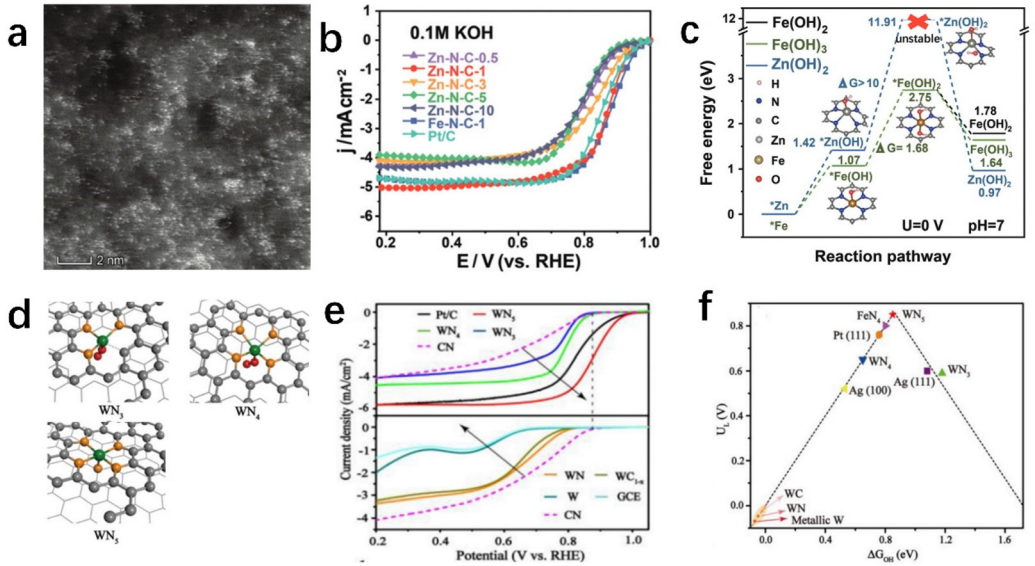

Fig. 16 (a and b) Aberration-corrected HAADF-STEM image and ORR polarization curve of the Zn–N–C-1. (c) Free-energy diagrams for $Zn(OH)_2$, $Fe(OH)_2$, and $Fe(OH)_3$. Reproduced with permission ref. 183. Copyright 2019, Wiley-VCH. (d and e) Schematic models and comparison of the ORR performances of WN_3, WN_4, and WN_5. (f) Illustration of the limiting potential (U_L) "volcano" as a function of the change in ΔG_{OH}. Reproduced with permission ref. 184. Copyright 2019, Elsevier.

$Mn–N_3O_1$ sites were subsequently produced by Yang *et al.*[189] With the addition of O atoms, the d-bind center may be moved to a better location, resulting in purposeful ORR dynamics. Mn metal is employed for ORR reactions in an acidic environment, just like other transition metals like Fe, Co, *etc*. In Fig. 17e, the Mn–N–C catalyst prepared in the study of Li *et al.*[190] showed excellent ORR activity in acidic conditions with $E_{1/2}$ = 0.80 V (Fig. 17f). The DFT calculations result were the same as those observed by XAS, and MnN_4 was the best active site (Fig. 17g). To prevent the oxidative corrosion of the catalyst caused by the Fenton reaction, Luo *et al.*[191] obtained a Cr–N–C catalyst (Fig. 17h and i). In acidic conditions, the $E_{1/2}$ reached 0.773 V in Fig. 17j. Additionally, Cr/N/C-950 showed greater ORR stability than Fe–N–C after 20 000 cycles, with just a 15 mV decrease in the $E_{1/2}$ being noticed (Fig. 17k). This also provided a new idea for solving the stability problem of traditional transition metal catalysts.

6. Carbon-based main-group metal catalysts

Through the continuous efforts of scientists, ORR catalysts with the main group metals (Mg, Al, Ca, *etc*.) as the active centers have also shown promising activities.

In contrast to precious metals and transition metals, the main group metals were often considered to be devoid of ORR catalytic activity.[192] However, in nature, enzymes that play a key role in many important metabolic pathways and nucleic acid biochemistry had been found to contain group metal magnesium (Mg) cofactors,[193,194] indicating that Mg metals have excellent potential to be used as efficient ORR catalysts. More recently, Bisen *et al.*[195] produced an Mg–N–C catalyst by a very simple method using only Mg precursor and dicyandiamide (DCDA) (Fig. 18a). The Mg–N–C catalyst had ORR performance (Fig. 18b). Excitingly, Mg–N–C also exhibited excellent cycling durability: in Fig. 18c there was a loss of 16 mV in $E_{1/2}$ after 10k cycles. Combined analysis by microscopy and spectroscopy confirmed that Mg–N–C was partially responsible for its high activity. Moreover, the ORR activity of Mg–N–C was proportional to the pyridine N and pyrrole N content at a certain ratio, and the defects on graphitic carbon also caused a faster electron transfer, which reduced the R_{ct} and enhanced the ORR activity. DFT calculations by Liu *et al.*[196] showed that the adsorption strength of oxygen intermediates on Mg is lower compared with Ca and Al, which were also main group metals. Additionally, the coordination of the main group metal Mg with N atoms can affect its catalytic activity, and Mg coordinated with two nitrogen atoms had close to optimal adsorption strength with intermediate oxygen species, thus obtaining the optimal ORR activity (Fig. 18d and e). To verify their calculations, Mg–N–C catalysts with MgN_2C were synthesized (Fig. 18f). In Fig. 18g, the $E_{1/2}$ of Mg–N–C was 0.91 V and the E_{onset} was 1.03 V. The above findings remind us that some methods that can enhance the ORR activity of transition metal–N–C can also be tried on the main group metals, which may lead to surprising discoveries.

Al is the most prevalent metal on Earth, and can be found everywhere in our daily life. And Al is in the same family as B with low electronegativity, so the vacant $3p_z$ orbital of Al can extract π electrons and form a positively charged Al active center like B.[197] When O_2 is adsorbed on Al, the O–O bond will

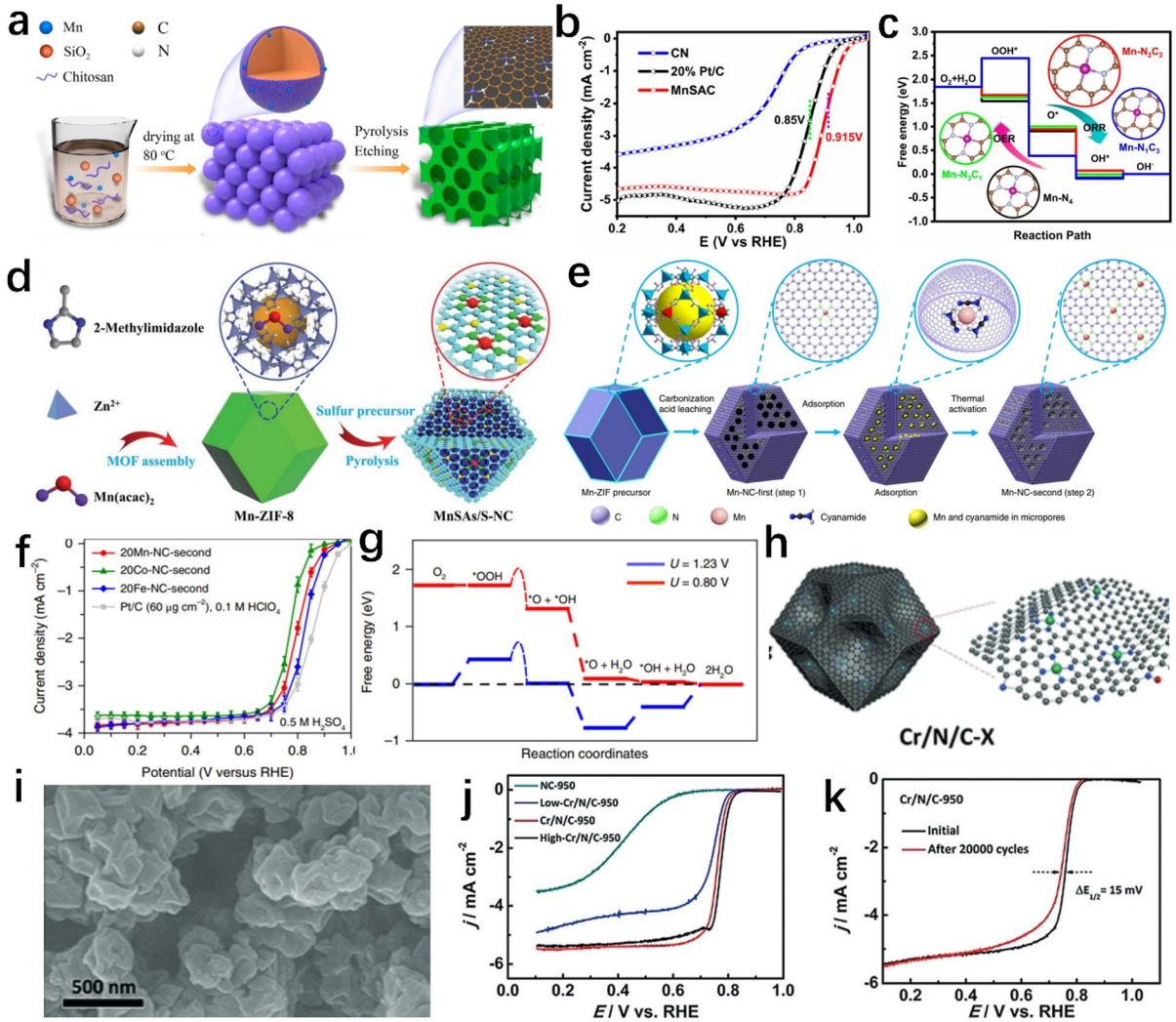

Fig. 17 (a–c) Schematic illustration for the preparation, ORR polarization curve, and theoretical ORR and OER activity of MnSAC. Reproduced with permission ref. 187. Copyright 2020, American Chemical Society. (d) Schematic illustration for the preparation of MnSAs/S–NC. Reproduced with permission ref. 188. Copyright 2020, The Royal Society of Chemistry. (e–g) Schematic illustration for the preparation, ORR polarization curves, and calculated free-energy evolution diagram of Mn-NC-second. Reproduced with permission ref. 190. Copyright 2018, Springer Nature. (h–k) Schematic illustration, SEM, ORR polarization curves, and durability tests of the Cr SACs. Reproduced with permission ref. 191. Copyright 2019, Wiley-VCH.

be longer, indicating that Al-doped graphene may have good ORR activity. Qin *et al.*[198] synthesized Al- and N-codoped graphene (ANG) by pyrolyzing Al precursor on N-doped graphene (NG) shown in Fig. 18h. It was found that ANG had an $E_{1/2}$ of 0.85 V. And ANG had excellent stability: after 20 000 s, as the current retention was 90%. Calculations, in Fig. 18i, found that among the three structures, *ortho*-ANG exhibited the lowest overpotential of *ortho*-, *meta*-, and *para*-ANG, demonstrating that the Al and N structure with direct bonding had the best performance and the lowest energy barrier. Liu *et al.*[199] used O to replace the coordinating N atom, which induces higher positive charge density in the Ca central atom (Fig. 18j). The DFT calculations showed that the introduction of oxygen changed the electronic structure of the Ca active center, which can enhance ORR activity by enhancing the adsorption of O intermediates. The highest $E_{1/2}$ = 0.90 V was in an alkaline environment.

These works demonstrate to us that the main-group-metal elements can be highly active and extremely durable ORR catalysts.

7. Carbon-based diatomic metal catalysts

SACs have been developed over decades[200–202] in many areas, such as electrocatalysis,[202,203] and photocatalysis.[204] However, there are still some disadvantages that hinder further development: because of the high surface energy, they are prone to agglomeration at high loadings. Therefore, the metal loading

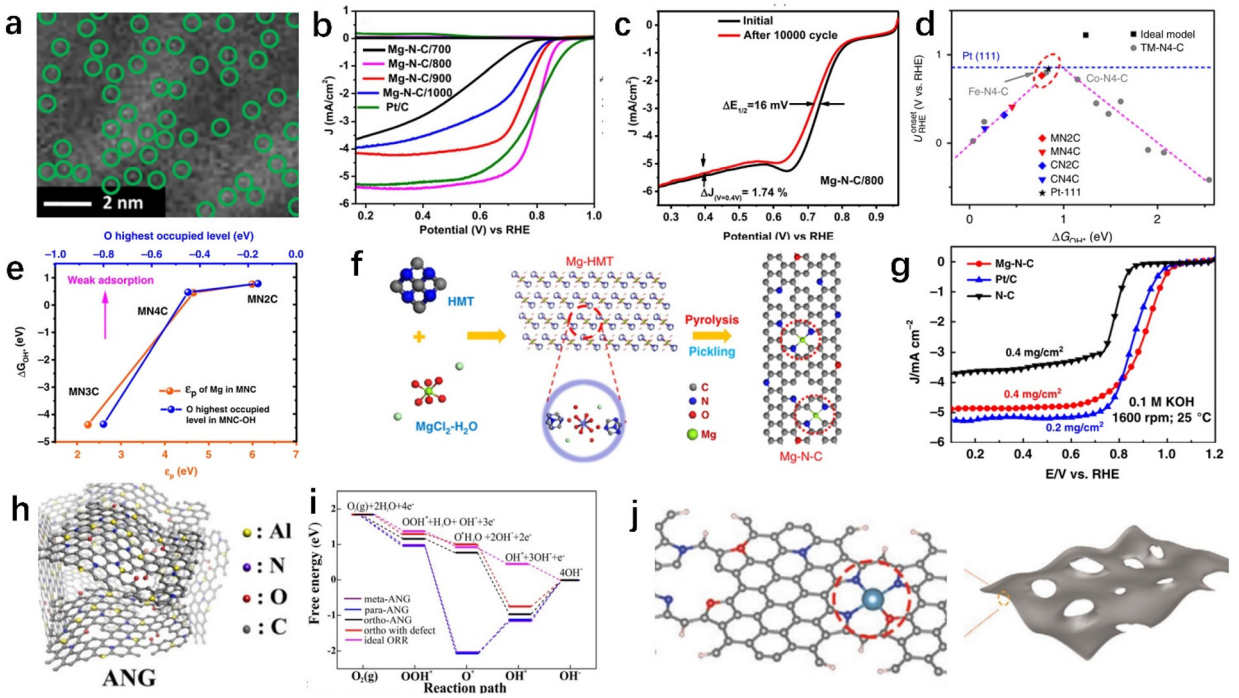

Fig. 18 (a–c) HAADF-STEM images, ORR polarization curves, and accelerated stability test of Mg–N–C/800. Reproduced with permission ref. 195. Copyright 2020, Elsevier. (d) The zoomed-in view of the onset potential *versus* ΔG_{OH*}. (e) Adsorption free energies of OH as a function of the εp position of metal atoms for Mg cofactors, and also as a function of the highest O-occupied state of hydroxyl after interaction. (f and g) Schematic illustration and LSV curve of Mg–N–C. Reproduced with permission ref. 196. Copyright 2020, Nature. (h and i) Schematic illustration, free-energy diagram of ANG. Reproduced with permission ref. 198. Copyright 2018, American Chemical Society. (j) Schematic illustration of the Ca-N,O/C. Reproduced with permission ref. 199. Copyright 2021, Wiley-VCH.

of SACs is usually limited to 1–2 wt%.[205] Moreover, there is only one kind of active site in SACs, and although the ORR performance can be enhanced through structural engineering, SACs have limited chance of exceeding their intrinsic activity limit. In recent years, research into diatomic catalysts has revealed that they not only inherit the advantages of SACs, but due to the synergy between different metals, it may be possible to achieve activities that are beyond the reach of monoatomic catalysts.[206]

7.1 Pt and transition metals

Pt SACs greatly improved the utilization of Pt metal. Although the introduction of non-metallic heteroatoms can improve the activity of Pt sites, this is still very limited. Using low-cost transition metals to construct low-platinum catalysts can not only significantly cut costs, but also doping metals to change the coordination structure of platinum can significantly increase catalyst performance. Due to the good synergistic effect between Co and Pt metal, Co metal and Pt are often doped to make the catalyst have better ORR performance. As shown in Fig. 19a, Xiong *et al.*[207] synthesized N-doped PtCo nanoparticles (PtCo@NC) with good performance (Pt@ZIF-67). The $E_{1/2}$ of PtCo@NC-10 in potassium perchlorate and potassium hydroxide solutions is 0.929 V and 0.925 V (Fig. 19b). And the mass activities of PtCo@NC-10 in $HClO_4$ and KOH solutions at 0.9 V were 0.82 A mg^{-1}_{Pt} and 0.80 A mg^{-1}_{Pt}, respectively (Fig. 19c). The unique hybrid structure also endows the PtCo@NC-10 catalyst with good cycling durability. In another study, the PtCo co-doped catalyst (LP@PF-2) prepared by Liu *et al.*[208] also had exciting ORR activity with $E_{1/2}$ = 0.959 V (Fig. 19d and e).

Zhang *et al.*[209] gained insight into the catalytic mechanism of their PtCo catalyst (A-CoPT-NC, Fig. 19f) by DFT calculations. After screening five different coordination structures, this revealed that the configuration with the lowest overpotential, a(Co–Pt)@N8V4, had the highest energy efficiency in Fig. 19g. The up-shifted d orbital in relation to the Fermi level will provide a strong binding between the catalyst and the adsorbate, and *vice versa*, according to the d band center theory of Nørskov *et al.*[210] It was clear that a(Co–Pt)@N8V4 and oxygen had a stronger link because the energy of the Co 3d orbital in this compound was closer to the Fermi level than the energy of the Pt 5d orbital in this compound. As shown in Fig. 19h, due to the asymmetric distribution of platinum and cobalt, which polarized the surface charge near the active sites, the O_2 reduction process will be accelerated by the electrons stored on the Co site, improving the ORR performance.

In addition to Co, scientists have doped other transition metal atoms (Cu, Fe, *etc.*) with Pt to obtain high-performance ORR catalysts. In Fig. 19i, Geng *et al.*[211] calcined the Cu-doped ZIF-8 material at high temperatures and later loaded it with Pt atoms in an oriented manner, resulting in Cu–Pt C-ZIF-CuPt.

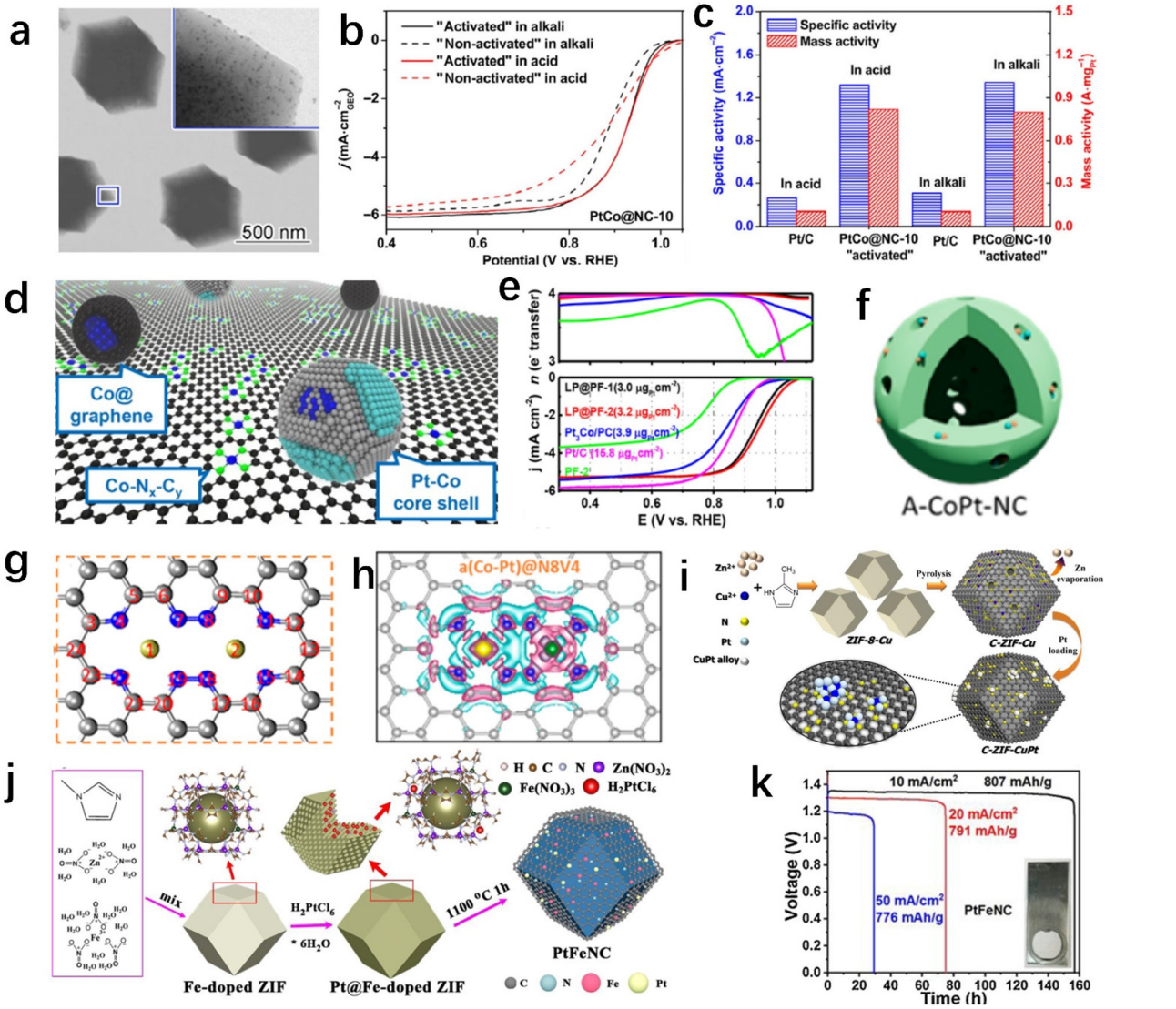

Fig. 19 (a–c) TEM images, the durability test, mass activity and specific activity of PtCo@NC-10. Reproduced with permission ref. 207. Copyright 2017, Tsinghua University Press. (d and e) Schematic illustration, LSV and the number of transferred electrons of LP@PF-2. Reproduced with permission ref. 208. Copyright 2018, AAAS. (f) Schematic illustration of A-CoPt-NC. (g and h) Model of the configuration and top view of the charge densities of a(Co–Pt)@N8V4. Reproduced with permission ref. 209. Copyright 2018, American Chemical Society. (i) C-ZIF-CuPt catalyst preparation process. Reproduced with permission ref. 211. Copyright 2021, Elsevier. (j) Schematic illustration of PtFeNC. (k) Specific capacities of primary ZAB based on PtFeNC. Reproduced with permission ref. 212. Copyright 2018, American Chemical Society.

The $E_{1/2}$ of C-ZIF-CuPt was 0.874 V (*vs.* RHE). Zhong *et al.*[212] encapsulated Pt into Fe-doped zeolite imidazolium salt skeleton cavities and subsequently obtained atomically dispersed PtFe SACs (PtFeNC) by subsequent pyrolysis (Fig. 19j). Importantly, the Zn–air battery (ZAB) showed a specific capacity of up to 807 mA h g^{-1} at a discharge current density of 10 mA cm^{-2} (Fig. 19k).

7.2 Transition metals and transition metals

Different transition metals can also provide surprising catalytic capabilities due to the synergy, such as Fe–Mn,[213–215] Fe–Co,[216–218] Fe–Ni,[219] Co–Ni,[220] and Co–Zn.[221,222] Being the most likely transition metal to replace widely used Pt/C catalysts, Fe is often used by scientists to prepare two-atom catalysts by co-doping with other transition metals. For example, Cai *et al.*[223] synthesized atomically dispersed iron–manganese binary catalysts (Fe&Mn/N–C) on N-doped graphitic carbon (Fig. 20a). The formation of MnN_4 sites modulated the local electron structure and density of FeN_4 active sites, leading to a significant improvement in ORR activity with $E_{1/2}$ = 0.904 V. And by forming a possible FeN_4–O–MnN_4 structure, more FeN_4 active sites were retained in the carbon carrier. As shown in Fig. 20b, according to DFT calculations, FeN4–O–MnN4 increased the ORR activity by lessening the ORR's overall energy barrier lowering.

Yang *et al.*[214] successfully prepared Fe,Mn/N–C electrocatalysts with bimetallic atom dispersion by implanting Mn–N in

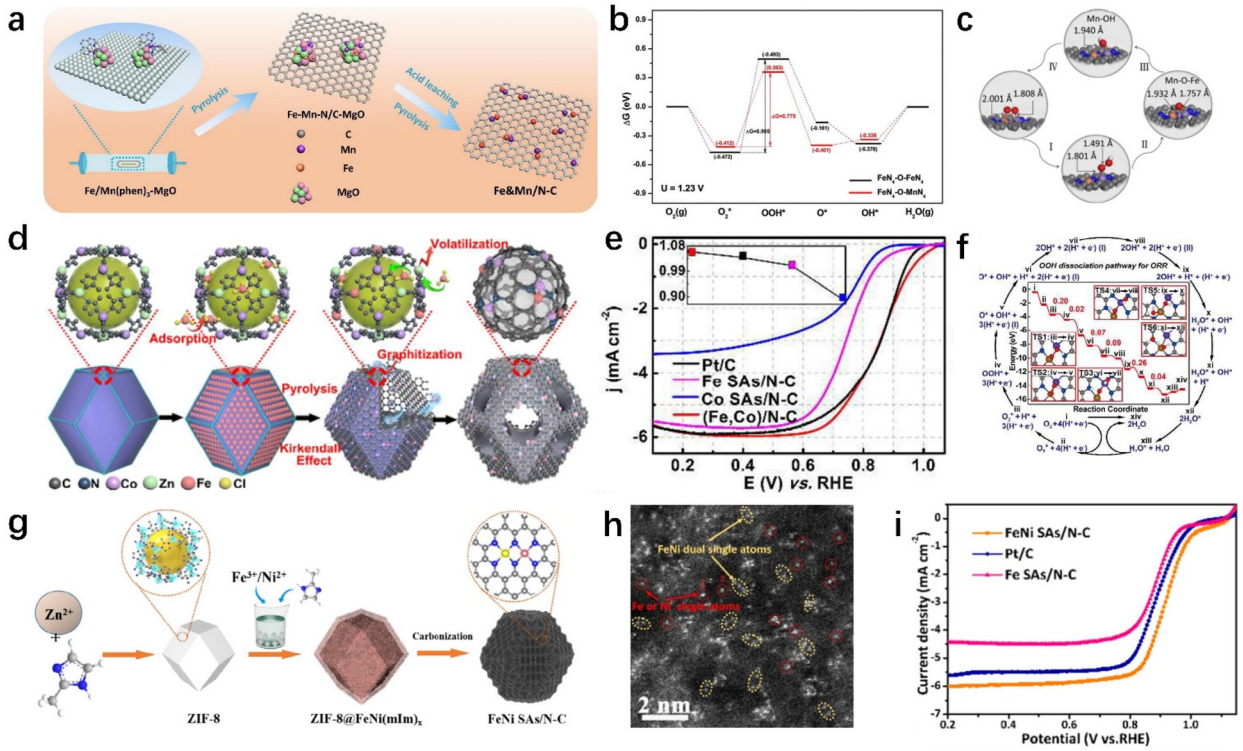

Fig. 20 (a and b) Schematic diagram and free energy evolution diagram of Fe&Mn/N–C. Reproduced with permission ref. 223. Copyright 2022, Wiley-VCH. (c) Optimized atomic structures of Fe,Mn/N–C. Reproduced with permission ref. 214. Copyright 2021, Springer. (d–f) Schematic illustration, RDE polarization curves, energies of intermediates and transition states in the mechanism of ORR of (Fe,Co)/N–C. Reproduced with permission ref. 224. Copyright 2017, American Chemical Society. (g–i) Graphic illustration, HAADF-STEM, and LSV polarization curve of FeNi SAs/NAC. Reproduced with permission ref. 225. Copyright 2022, Elsevier.

Fe/N–C through pre-polymerization and pyrolysis processes. Similar to the Fe&Mn/N–C prepared by Cai *et al.*,[223] it showed an excellent ORR performance ($E_{1/2}$ = 0.928 V in 0.1 M KOH and $E_{1/2}$ = 0.804 V in 0.1 M $HClO_4$). The results of DFT calculations showed that when O_2 is adsorbed by Fe/Mn atom partners, it led to suitable bond lengths and suitable binding energies, thus reducing the dissociation energy barrier (Fig. 20c). Additionally, it can quickly break the bonds between M–OH and efficiently capture oxygen-containing intermediates, ensuring the regeneration of O* and OH* intermediates and boosting ORR kinetics by effectively reducing peroxide formation.

In another study, in Fig. 20d, Wang *et al.*[224] constructed (Fe,Co)/N–C catalysts with Fe–Co double sites embedded on N-doped porous carbon. These exhibited excellent ORR performance ($E_{1/2}$ = 0.863 V, Fig. 20e). More importantly, the activity of (Fe,Co)/N–C was significantly higher than that of the single active metal Fe–N_x–C and Co–N_x–C, indicating that the Fe,Co bimetallic site plays a key role in the ORR reaction. As shown in Fig. 20f, DFT calculations showed that the O–O bond was more prone to break due to the strong binding of O_2 on the Fe–Co dual site. Besides, the potential barriers for the dissociation of O_2 and OOH* into O* and OH* were lower than those of Fe–N_x–C and Co–N_x–C, which is consistent with the experimental results.

FeNi SAs/NAC catalysts were obtained from the pyrolysis of ZIF-8@FeNi$(mIm)_x$ precursor by Bai *et al.*[225] (Fig. 20g). HAADF-STEM results showed that FeNi diatoms and Fe or Ni single atoms were distributed evenly on N-doped carbon (Fig. 20h). Consequently, the $E_{1/2}$ of FeNi SAs/NAC was 0.91 V in 0.1 M KOH (Fig. 20i). The Fe/Ni metal 3d orbital interaction was considered to be the cause of its exceptional ORR activity. Furthermore, the Bader charge of Fe with Ni is higher than that of Fe without Ni, implying an electron transfer occurring between Fe and Ni. Furthermore, the FeNi SAs/NAC catalysts showed faster ORR dynamics in the RDS of four-electron transfer.

Bi element can effectively optimize the activity of peroxides and noble metals, but it is quite uncommon for it to increase the oxygen reduction activity of SACs catalysts. Jin *et al.*[226] successfully synthesized a Fe/N–C catalyst with Bi–O forms (Fe/Bi-RNC) by using rod-like C_3N_4 templates (Fig. 21a). Due to its porous rod-like structure, the RNC not only exposed numerous active sites, but also facilitated charge transport. Also, the additional nitrogen doping introduced by the C_3N_4 template facilitates improved the redox kinetics of the carbon material. The optimal Fe/Bi-RNC catalyst had an $E_{1/2}$ of 0.899 V (Fig. 21b). According to the calculations of DFT in Fig. 21c, the presence of Bi–O adjusts the electronic structure of Fe–N_4–BiO, resulting in a significant reduction of the band gap and their

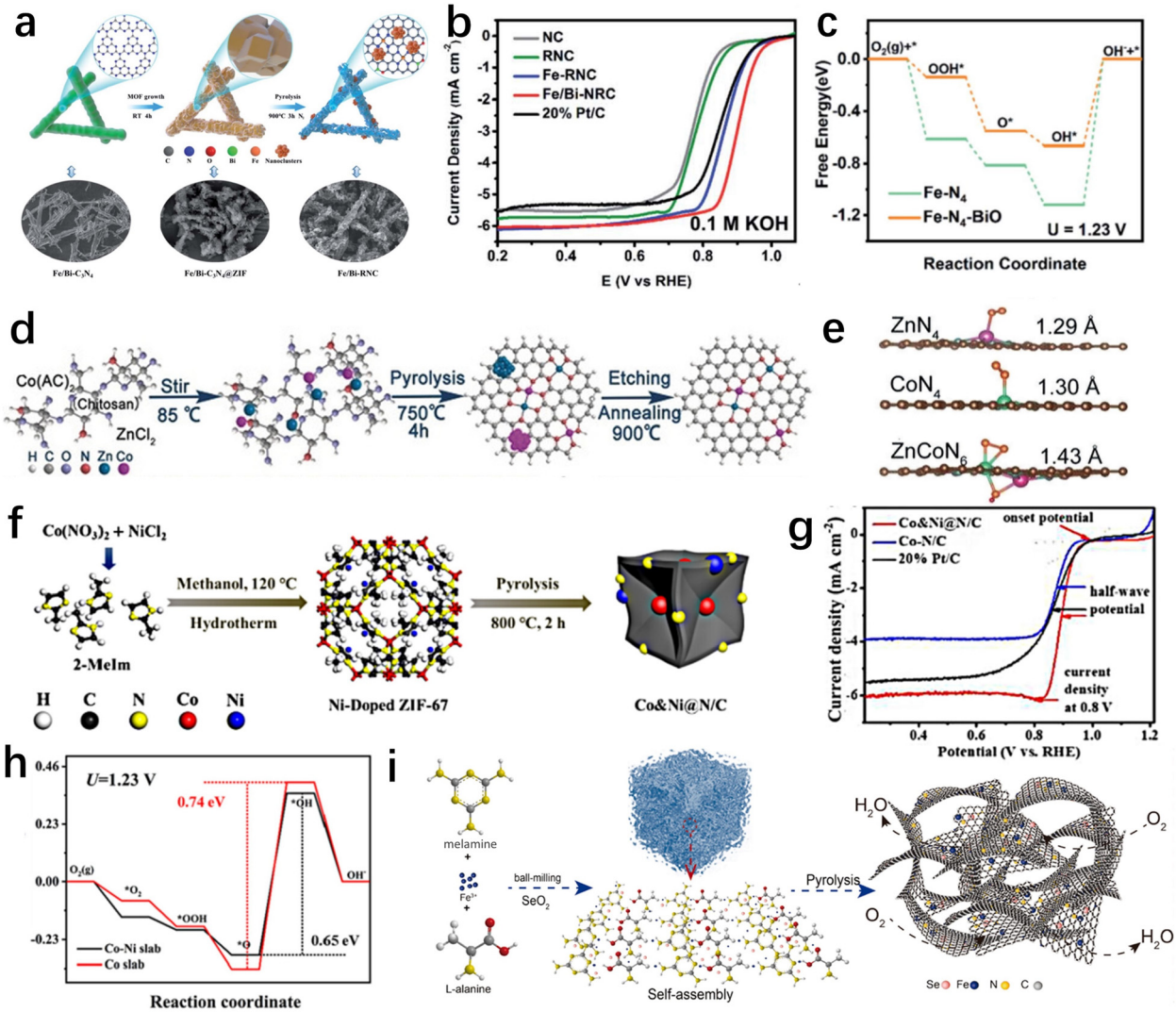

Fig. 21 (a–c) Preparation process, LSV curve, and ORR free energy diagram of Fe/Bi-RNC. Reproduced with permission ref. 226. Copyright 2022, Royal Society of Chemistry. (d) Illustration of the formation of Zn/CoN-C. (e) Optimized geometry of O_2 adsorption configuration on the ZnN_4, CoN_4, and $ZnCoN_6$(OH) systems. Reproduced with permission ref. 221. Copyright 2019, Wiley-VCH. (f–h) Proposed synthetic protocol, LSV curve, and free energy diagram of Co&Ni@N/C. Reproduced with permission ref. 220. Copyright 2019, Science Press and Dalian Institute of Chemical Physics. (i) Schematic illustration of Fe_1Se_1-NC. Reproduced with permission ref. 227. Copyright 2022, Elsevier.

synergistic impact speeds up the electron transfer in the step that determines the ORR rate, leading to a better oxygen reduction performance.

In addition to the diatomic catalysts involving Fe, other combinations were found to have excellent ORR activity as well. In Fig. 21d, the Zn/Co–N–C catalyst prepared by Lu *et al.*[221] exhibited high ORR performance with an $E_{1/2}$ of 0.861 V. It was found that the electronic structure was adjusted due to the co-coordination of bimetallic Zn and Co with N and the distance between the O–O bonds increased, leading to easier cracking and thus enhanced ORR activity (Fig. 21e). In another research study, Mao *et al.*[220] prepared Ni-doped Co–N/C catalysts using Ni-doped ZIF-67 as a precursor (Fig. 21f). In Fig. 21g, the Ni&Co@N/C exhibited an $E_{1/2}$ of 0.895 V. The PDS of the $4e^-$ ORR process was lowered by the synergy of Ni–Co bimetals according to calculations using DFT, and the adsorption energy on the catalyst surface was reduced due to the introduction of nickel metal (Fig. 21h).

7.3 Metals and non-metals

In the past, scientists have focused their research on the construction of bimetallic atomic pairs. However, a recent study by Chen *et al.*[227] had made people rethink this issue (Fig. 21i). They constructed Fe/Se diatomic catalysts, which contain asymmetrically coordinated Fe–N_5 molecules and SeC_2 binary sites. Not only did Se atoms enhance their ORR activity through synergistic interactions with the Fe active site, but Se single-atom sites also exhibited significant ORR activity. As a result, the Fe_1Se_1-NC catalyst showed an ORR activity beyond that of Pt/C (E_{onset}, 1.0 V *vs.* 0.98 V). Spectroscopic characteriz-

ation studies and theoretical calculations confirmed that the introduction of Se has multiple effects, which can provide new active sites and effectively tune charge redistribution and the spin state of the Fe active site, providing a new idea for improving the synthesis of diatomic catalysts.

8. Summary and outlook

SACs are considered promising candidates for ORR because of their maximum atom utilization and high catalytic activity. This review summarizes the effective methods for coordination engineering by examining the latest literature, including the selection of central atoms, the number and type of coordinating nitrogen atoms, the coordination of non-metallic heteroatoms, and the development of bimetallic catalysts. Both experiments and theoretical calculations show that these methods can significantly increase the ORR activity of SACs. Although great progress has been made, there are still some problems preventing the further development of carbon-based SACs. Here we have listed some of the most important issues and proposed solutions.

1. Lack of advanced characterization techniques. Various analysis techniques have been used to characterize the fine structure of single-atom active centers, but they can only get an average coordination structure. The local structure of the single metal sites still vague. If metal centers with different coordination modes are present in one catalyst at the same time, it is difficult to determine the true active center. DFT calculations are often used to explore the reaction mechanisms of SACs in depth. However, the construction of accurate theoretical models also requires a defined local structure. Therefore, the development of more advanced and accurate characterization techniques is necessary to deeply explore the structure and mechanism of SACs.

2. The controllable synthesis of SACs is difficult. Although many effective methods such as coprecipitation, wet impregnation, *etc*., have been developed to prepare SACs, with the existing synthesis methods it is difficult to precisely synthesize the desired coordination configurations. Additionally, the increase of metal amount during the synthesis process can easily lead to aggregation, which hinders the preparation of high-density active sites. To resolve these limitations, new synthesis strategies should be developed to better control the structure of the SACs and increase the density of active sites.

3. There is still a gap to actual applications. Although the ORR activity and stability of SACs are now substantially improved, there are still a number of problems in practical applications, such as sluggish mass transport, large resistance, poor durability, low catalytic activity in acidic conditions, *etc*., which makes them even more limited in application. Therefore, more advanced SACs should be developed to meet the industrial demand.

4. More efficient support should be developed. For an electrocatalyst, on the one hand, the support can play the role of dispersing the metal active centers. On the other hand, the inherent properties of the support, such as the structure, specific surface area, electrical conductivity and stability have a significant impact on the catalytic performance. Therefore, selecting the appropriate support is critical for increasing the catalytic performance of SACs. Currently, carbon-based materials are the most commonly used support for SACs. More excellent materials with the characters of better electrical conductivity, a larger specific surface area and greater stability than the carbon-based materials should be explored to support SACs.

Conflicts of interest

There are no conflicts to declare.

Acknowledgements

The authors thank the National Natural Science Foundation of China (Grants No. 22201262, U22A20143), Zhongyuan Science and Technology Innovation Leading Talent Project (224200510005), Natural Science Foundation of Henan Province (222300420290) and China Postdoctoral Science Foundation (2021M702939). The authors thank Modern Analysis and Gene Sequencing Center of Zhengzhou University for helping characterization.

References

1 H. Jin, C. Guo, X. Liu, J. Liu, A. Vasileff, Y. Jiao, Y. Zheng and S.-Z. Qiao, *Chem. Rev.*, 2018, **118**, 6337–6408.
2 A. Kulkarni, S. Siahrostami, A. Patel and J. K. Nørskov, *Chem. Rev.*, 2018, **118**, 2302–2312.
3 M. L. Pegis, C. F. Wise, D. J. Martin and J. M. Mayer, *Chem. Rev.*, 2018, **118**, 2340–2391.
4 M. Borghei, J. Lehtonen, L. Liu and O. J. Rojas, *Adv. Mater.*, 2018, **30**, 1703691.
5 S. Hienuki, H. Mitoma, M. Ogata, I. Uchida and S. Kagawa, *Int. J. Hydrogen Energy*, 2021, **46**, 36569–36580.
6 Z. Li, G. Su and L. Zheng, *Int. J. Hydrogen Energy*, 2021, **46**, 12784–12800.
7 V. Oldenbroek, G. Smink, T. Salet and A. J. M. van Wijk, *Appl. Sci.*, 2020, **10**, 143.
8 S. Guo, S. Zhang and S. Sun, *Angew. Chem., Int. Ed.*, 2013, **52**, 8526–8544.
9 M. Winter and R. J. Brodd, *Chem. Rev.*, 2004, **104**, 4245–4270.
10 T. S. Andrade, M. C. Pereira and P. Lianos, *J. Electroanal. Chem.*, 2020, **878**, 114559.
11 Z. Li, M. Shao, L. Zhou, R. Zhang, C. Zhang, M. Wei, D. G. Evans and X. Duan, *Adv. Mater.*, 2016, **28**, 2337–2344.
12 X. Wan, X. Liu, Y. Li, R. Yu, L. Zheng, W. Yan, H. Wang, M. Xu and J. Shui, *Nat. Catal.*, 2019, **2**, 259–268.

13 C. Zhang and K. Huang, *Adv. Energy Mater.*, 2020, **11**, 2000630.
14 H. Zhang, M. Zhao, H. Liu, S. Shi, Z. Wang, B. Zhang, L. Song, J. Shang, Y. Yang, C. Ma, L. Zheng, Y. Han and W. Huang, *Nano Lett.*, 2021, **21**, 2255–2264.
15 Y. Nie, L. Li and Z. Wei, *Chem. Soc. Rev.*, 2015, **44**, 2168–2201.
16 J. C. Carrillo-Rodríguez, A. M. Garay-Tapia, B. Escobar-Morales, J. Escorcia-García, M. T. Ochoa-Lara, F. J. Rodríguez-Varela and I. L. Alonso-Lemus, *Int. J. Hydrogen Energy*, 2021, **46**, 26087–26100.
17 X. Wang, J. Zhou, H. Fu, W. Li, X. Fan, G. Xin, J. Zheng and X. Li, *J. Mater. Chem. A*, 2014, **2**, 14064–14070.
18 Y. Chen, R. Gao, S. Ji, H. Li, K. Tang, P. Jiang, H. Hu, Z. Zhang, H. Hao, Q. Qu, X. Liang, W. Chen, J. Dong, D. Wang and Y. Li, *Angew. Chem., Int. Ed.*, 2021, **60**, 3212–3221.
19 Y. Zhang, N. Zhang, P. Wang, L. Shen, K. Li, S. Li, M. Yang and P. He, *Int. J. Hydrogen Energy*, 2022, **47**, 5474–5485.
20 S. Chen, Q. Chen, S. Ding, Y. Tian, J. Wang, S. Hou and J. Zhang, *Nano Res.*, 2022, DOI: **10.1007/s12274-022-5247-9**.
21 J. K. Dombrovskis and A. E. C. Palmqvist, *Fuel Cells*, 2016, **16**, 4–22.
22 H. Y. Kim, J. M. Kim, Y. Ha, J. Woo, A. Byun, T. J. Shin, K. H. Park, H. Y. Jeong, H. Kim, J. Y. Kim and S. H. Joo, *ACS Catal.*, 2019, **9**, 11242–11254.
23 F. Kong, Z. Ren, M. Norouzi Banis, L. Du, X. Zhou, G. Chen, L. Zhang, J. Li, S. Wang, M. Li, K. Doyle-Davis, Y. Ma, R. Li, A. Young, L. Yang, M. Markiewicz, Y. Tong, G. Yin, C. Du, J. Luo and X. Sun, *ACS Catal.*, 2020, **10**, 4205–4214.
24 S. Zhang, Y. Shao, G. Yin and Y. Lin, *J. Mater. Chem. A*, 2013, **1**, 4631–4641.
25 W. Wu, Z. Zhang, Z. Lei, X. Wang, Y. Tan, N. Cheng and X. Sun, *ACS Appl. Mater. Interfaces*, 2020, **12**, 10359–10368.
26 Y. Wang, D. F. Ruiz Diaz, K. S. Chen, Z. Wang and X. C. Adroher, *Mater. Today*, 2020, **32**, 178–203.
27 H. S. Wroblowa, P. Yen Chi and G. Razumney, *J. Electroanal. Chem. Interfacial Electrochem.*, 1976, **69**, 195–201.
28 C.-W. Ye and L. Xu, *J. Mater. Chem. A*, 2021, **9**, 22218–22247.
29 B. Qiao, A. Wang, X. Yang, L. F. Allard, Z. Jiang, Y. Cui, J. Liu, J. Li and T. Zhang, *Nat. Chem.*, 2011, **3**, 634–641.
30 P. Liu, Y. Zhao, R. Qin, S. Mo, G. Chen, L. Gu, D. M. Chevrier, P. Zhang, Q. Guo, D. Zang, B. Wu, G. Fu and N. Zheng, *Science*, 2016, **352**, 797–800.
31 L. Peng, L. Shang, T. Zhang and G. I. N. Waterhouse, *Adv. Energy Mater.*, 2020, **10**, 2003018.
32 F. Li, G.-F. Han, H.-J. Noh, S.-J. Kim, Y. Lu, H. Y. Jeong, Z. Fu and J.-B. Baek, *Energy Environ. Sci.*, 2018, **11**, 2263–2269.
33 P. Song, M. Luo, X. Liu, W. Xing, W. Xu, Z. Jiang and L. Gu, *Adv. Funct. Mater.*, 2017, **27**, 1700802.
34 C. Zhu, S. Fu, Q. Shi, D. Du and Y. Lin, *Angew. Chem., Int. Ed.*, 2017, **56**, 13944–13960.
35 Y. Chen, S. Ji, C. Chen, Q. Peng, D. Wang and Y. Li, *Joule*, 2018, **2**, 1242–1264.
36 T. Sun, L. Xu, D. Wang and Y. Li, *Nano Res.*, 2019, **12**, 2067–2080.
37 J. Liu, *ACS Catal.*, 2017, **7**, 34–59.
38 R. Lang, W. Xi, J.-C. Liu, Y.-T. Cui, T. Li, A. F. Lee, F. Chen, Y. Chen, L. Li, L. Li, J. Lin, S. Miao, X. Liu, A.-Q. Wang, X. Wang, J. Luo, B. Qiao, J. Li and T. Zhang, *Nat. Commun.*, 2019, **10**, 234.
39 J. Yang, W. Li, D. Wang and Y. Li, *Adv. Mater.*, 2020, **32**, 2003300.
40 A. Wang, J. Li and T. Zhang, *Nat. Rev. Chem.*, 2018, **2**, 65–81.
41 Y. Ying, K. Fan, X. Luo, J. Qiao and H. Huang, *J. Mater. Chem. A*, 2021, **9**, 16860–16867.
42 Y. Gao, Z. Cai, X. Wu, Z. Lv, P. Wu and C. Cai, *ACS Catal.*, 2018, **8**, 10364–10374.
43 L. Zhang, Y. Zhao, M. N. Banis, K. Adair, Z. Song, L. Yang, M. Markiewicz, J. Li, S. Wang, R. Li, S. Ye and X. Sun, *Nano Energy*, 2019, **60**, 111–118.
44 B.-J. Su, K.-W. Wang, C.-J. Tseng, C.-W. Pao, J.-L. Chen, K.-T. Lu and J.-M. Chen, *ACS Appl. Mater. Interfaces*, 2020, **12**, 24710–24716.
45 S. Fu, C. Zhu, J. Song, D. Du and Y. Lin, *Adv. Energy Mater.*, 2017, **7**, 1700363.
46 J. Hu, W. Liu, C. Xin, J. Guo, X. Cheng, J. Wei, C. Hao, G. Zhang and Y. Shi, *J. Mater. Chem. A*, 2021, **9**, 24803–24829.
47 X. Wang, Z. Li, Y. Qu, T. Yuan, W. Wang, Y. Wu and Y. Li, *Chem*, 2019, **5**, 1486–1511.
48 C. Yang, X. Ma, J. Zhou, Y. Zhao, X. Xiang, H. Shang and B. Zhang, *Int. J. Hydrogen Energy*, 2022, **47**, 21634–21661.
49 H. Shang and D. Liu, *Nano Res.*, 2023, DOI: **10.1007/s12274-023-5449-9**.
50 Z. Li, S. Ji, Y. Liu, X. Cao, S. Tian, Y. Chen, Z. Niu and Y. Li, *Chem. Rev.*, 2020, **120**, 623–682.
51 S. Ji, Y. Chen, X. Wang, Z. Zhang, D. Wang and Y. Li, *Chem. Rev.*, 2020, **120**, 11900–11955.
52 S. Yang, J. Kim, Y. J. Tak, A. Soon and H. Lee, *Angew. Chem., Int. Ed.*, 2016, **55**, 2058–2062.
53 R. T. Hannagan, G. Giannakakis, M. Flytzani-Stephanopoulos and E. C. H. Sykes, *Chem. Rev.*, 2020, **120**, 12044–12088.
54 M. Wang, S. Liu, T. Qian, J. Liu, J. Zhou, H. Ji, J. Xiong, J. Zhong and C. Yan, *Nat. Commun.*, 2019, **10**, 341.
55 K. Wu, X. Chen, S. Liu, Y. Pan, W.-C. Cheong, W. Zhu, X. Cao, R. Shen, W. Chen, J. Luo, W. Yan, L. Zheng, Z. Chen, D. Wang, Q. Peng, C. Chen and Y. Li, *Nano Res.*, 2018, **11**, 6260–6269.
56 H. Zhong, C. Shi, J. Li, R. Yu, Q. Yu, H. Liu, Y. Yao, J. Wu, L. Zhou and L. Mai, *Chem. Commun.*, 2020, **56**, 4488–4491.
57 T. Wang, X. Cao, H. Qin, L. Shang, S. Zheng, F. Fang and L. Jiao, *Angew. Chem., Int. Ed.*, 2021, **60**, 21237–21241.
58 H. Wang, Y. Zhao, J. Li, X. Wang, M. Huang, L. Zhang and C. Zhao, *Small Struct.*, 2023, 2300007.

59 L. Dong, J. Zang, W. Wang, X. Liu, Y. Zhang, J. Su, Y. Wang, X. Han and J. Li, *J. Colloid Interface Sci.*, 2020, **564**, 134–142.
60 S. Li, P. Zhang, Y. Wang, H. Sarvari, D. Liu, J. Wu, Y. Yang, Z. Wang and Z. D. Chen, *Nano Res.*, 2017, **10**, 1092–1103.
61 L. Zhang, L. Han, H. Liu, X. Liu and J. Luo, *Angew. Chem., Int. Ed.*, 2017, **56**, 13694–13698.
62 H. Shang, Z. Jiang, D. Zhou, J. Pei, Y. Wang, J. Dong, X. Zheng, J. Zhang and W. Chen, *Chem. Sci.*, 2020, **11**, 5994–5999.
63 X. Li, H. Rong, J. Zhang, D. Wang and Y. Li, *Nano Res.*, 2020, **13**, 1842–1855.
64 Y. He, S. Liu, C. Priest, Q. Shi and G. Wu, *Chem. Soc. Rev.*, 2020, **49**, 3484–3524.
65 H. Shang, W. Sun, R. Sui, J. Pei, L. Zheng, J. Dong, Z. Jiang, D. Zhou, Z. Zhuang, W. Chen, J. Zhang, D. Wang and Y. Li, *Nano Lett.*, 2020, **20**, 5443–5450.
66 D. Deng, X. Chen, L. Yu, X. Wu, Q. Liu, Y. Liu, H. Yang, H. Tian, Y. Hu, P. Du, R. Si, J. Wang, X. Cui, H. Li, J. Xiao, T. Xu, J. Deng, F. Yang, P. N. Duchesne, P. Zhang, J. Zhou, L. Sun, J. Li, X. Pan and X. Bao, *Sci. Adv.*, 2015, **1**, e1500462.
67 A. Franco, J. Á. Salatti-Dorado, V. García-Caballero, S. Lorca, L. Camacho, M. Cano, A. J. Fernández-Romero, J. J. Delgado, J. J. Giner-Casares and C. Carrillo-Carrión, *J. Mater. Chem. A*, 2022, **10**, 24590–24597.
68 H. Yang, H. Huang, Q. Wang, L. Shang, T. Zhang and S. Wang, *J. Mater. Chem. A*, 2023, **11**, 6191–6197.
69 X. Li, X. Yang, J. Zhang, Y. Huang and B. Liu, *ACS Catal.*, 2019, **9**, 2521–2531.
70 T. Zheng, X. Han, J. Wang and Z. Xia, *Nanoscale*, 2022, **14**, 16286–16294.
71 M. Xiao, J. Zhu, L. Ma, Z. Jin, J. Ge, X. Deng, Y. Hou, Q. He, J. Li, Q. Jia, S. Mukerjee, R. Yang, Z. Jiang, D. Su, C. Liu and W. Xing, *ACS Catal.*, 2018, **8**, 2824–2832.
72 W. Liu, Y. Chen, H. Qi, L. Zhang, W. Yan, X. Liu, X. Yang, S. Miao, W. Wang, C. Liu, A. Wang, J. Li and T. Zhang, *Angew. Chem., Int. Ed.*, 2018, **57**, 7071–7075.
73 J. Li, W. Xia, J. Tang, Y. Gao, C. Jiang, Y. Jia, T. Chen, Z. Hou, R. Qi, D. Jiang, T. Asahi, X. Xu, T. Wang, J. He and Y. Yamauchi, *J. Am. Chem. Soc.*, 2022, **144**, 9280–9291.
74 N. Li, L. Li, J. Xia, M. Arif, S. Zhou, F. Yin, G. He and H. Chen, *J. Mater. Sci. Technol.*, 2023, **139**, 224–231.
75 B. Yang, X. Li, Q. Cheng, X. Jia, Y. Liu and Z. Xiang, *Nano Energy*, 2022, **101**, 107565.
76 J. Zhang, Y. Zhao, C. Chen, Y.-C. Huang, C.-L. Dong, C.-J. Chen, R.-S. Liu, C. Wang, K. Yan, Y. Li and G. Wang, *J. Am. Chem. Soc.*, 2019, **141**, 20118–20126.
77 L. Peng, J. Yang, Y. Yang, F. Qian, Q. Wang, D. Sun-Waterhouse, L. Shang, T. Zhang and G. I. N. Waterhouse, *Adv. Mater.*, 2022, e2202544, DOI: **10.1002/adma.202202544**.
78 K. Yuan, D. Lutzenkirchen-Hecht, L. Li, L. Shuai, Y. Li, R. Cao, M. Qiu, X. Zhuang, M. K. H. Leung, Y. Chen and U. Scherf, *J. Am. Chem. Soc.*, 2020, **142**, 2404–2412.
79 Y. Guo, P. Yuan, J. Zhang, Y. Hu, I. S. Amiinu, X. Wang, J. Zhou, H. Xia, Z. Song, Q. Xu and S. Mu, *ACS Nano*, 2018, **12**, 1894–1901.
80 J. Zhang, M. Zhang, Y. Zeng, J. Chen, L. Qiu, H. Zhou, C. Sun, Y. Yu, C. Zhu and Z. Zhu, *Small*, 2019, **15**, e1900307.
81 P. Chen, T. Zhou, L. Xing, K. Xu, Y. Tong, H. Xie, L. Zhang, W. Yan, W. Chu, C. Wu and Y. Xie, *Angew. Chem., Int. Ed.*, 2017, **56**, 610–614.
82 W. Zhang, K. Mao and X. C. Zeng, *ACS Sustainable Chem. Eng.*, 2019, **7**, 18711–18717.
83 H. Sun, M. Wang, X. Du, Y. Jiao, S. Liu, T. Qian, Y. Yan, C. Liu, M. Liao, Q. Zhang, L. Meng, L. Gu, J. Xiong and C. Yan, *J. Mater. Chem. A*, 2019, **7**, 20952–20957.
84 Q. Li, W. Chen, H. Xiao, Y. Gong, Z. Li, L. Zheng, X. Zheng, W. Yan, W. C. Cheong, R. Shen, N. Fu, L. Gu, Z. Zhuang, C. Chen, D. Wang, Q. Peng, J. Li and Y. Li, *Adv. Mater.*, 2018, **30**, 1800588.
85 P. Chen, T. Zhou, L. Xing, K. Xu, Y. Tong, H. Xie, L. Zhang, W. Yan, W. Chu, C. Wu and Y. Xie, *Angew. Chem., Int. Ed.*, 2017, **56**, 610–614.
86 T. Liu, X.-J. Du, S. Li, Q.-L. Wu, Q. Guo, Z.-Z. Liu, J.-P. Zhao and F.-C. Liu, *Nanoscale*, 2022, **14**, 14248–14254.
87 J. Ding, D. Wu, S. Huang, C. Lu, Y. Chen, J. Zhang, L. Zhang, J. Li, C. Ke, D. Tranca, E. Kymakis and X. Zhuang, *Nanoscale*, 2021, **13**, 13249–13255.
88 X. Zhao, S. Takao, Y. Yoshida, T. Kaneko, T. Gunji, K. Higashi, T. Uruga and Y. Iwasawa, *Appl. Catal., B*, 2023, **324**, 122268.
89 S. Yuan, J. Zhang, L. Hu, J. Li, S. Li, Y. Gao, Q. Zhang, L. Gu, W. Yang, X. Feng and B. Wang, *Angew. Chem., Int. Ed.*, 2021, **60**, 21685–21690.
90 M. Wang, L. Cao, X. Du, Y. Zhang, F. Jin, M. Zhang, Z. Li and K. Su, *ACS Appl. Mater. Interfaces*, 2022, **14**, 25427–25438.
91 L. Zong, K. Fan, W. Wu, L. Cui, L. Zhang, B. Johannessen, D. Qi, H. Yin, Y. Wang, P. Liu, L. Wang and H. Zhao, *Adv. Funct. Mater.*, 2021, **31**, 2104864.
92 L. Cui, J. Zhao, G. Liu, Z. Wang, B. Li and L. Zong, *J. Colloid Interface Sci.*, 2022, **622**, 209–217.
93 Y. Nie, L. Li and Z. Wei, *Chem. Soc. Rev.*, 2015, **44**, 2168–2201.
94 W. Xia, A. Mahmood, Z. Liang, R. Zou and S. Guo, *Angew. Chem., Int. Ed.*, 2016, **55**, 2650–2676.
95 X. Zhou, J. Qiao, L. Yang and J. Zhang, *Adv. Energy Mater.*, 2014, **4**, 1301523.
96 T. Li, J. Liu, Y. Song and F. Wang, *ACS Catal.*, 2018, **8**, 8450–8458.
97 J. Liu, M. Jiao, L. Lu, H. M. Barkholtz, Y. Li, Y. Wang, L. Jiang, Z. Wu, D. J. Liu, L. Zhuang, C. Ma, J. Zeng, B. Zhang, D. Su, P. Song, W. Xing, W. Xu, Y. Wang, Z. Jiang and G. Sun, *Nat. Commun.*, 2017, **8**, 15938.
98 Z. Song, Y. N. Zhu, H. Liu, M. N. Banis, L. Zhang, J. Li, K. Doyle-Davis, R. Li, T. K. Sham, L. Yang, A. Young, G. A. Botton, L. M. Liu and X. Sun, *Small*, 2020, **16**, e2003096.

99 X. Zhu, X. Tan, K. H. Wu, S. C. Haw, C. W. Pao, B. J. Su, J. Jiang, S. C. Smith, J. M. Chen, R. Amal and X. Lu, *Angew. Chem., Int. Ed.*, 2021, **60**, 21911–21917.
100 Y. Chen, X. Zheng, J. Cai, G. Zhao, B. Zhang, Z. Luo, G. Wang, H. Pan and W. Sun, *ACS Catal.*, 2022, **12**, 7406–7414.
101 J. Zhao, C. Fu, K. Ye, Z. Liang, F. Jiang, S. Shen, X. Zhao, L. Ma, Z. Shadike, X. Wang, J. Zhang and K. Jiang, *Nat. Commun.*, 2022, **13**, 685.
102 M. Zhou, J. Guo and J. Fang, *Small Struct.*, 2022, **3**, 2100188.
103 M. Xiao, J. Zhu, G. Li, N. Li, S. Li, Z. P. Cano, L. Ma, P. Cui, P. Xu, G. Jiang, H. Jin, S. Wang, T. Wu, J. Lu, A. Yu, D. Su and Z. Chen, *Angew. Chem., Int. Ed.*, 2019, **58**, 9640–9645.
104 L. Cui, K. Fan, L. Zong, F. Lu, M. Zhou, B. Li, L. Zhang, L. Feng, X. Li, Y. Chen and L. Wang, *Energy Storage Mater.*, 2022, **44**, 469–476.
105 C. Zhang, J. Sha, H. Fei, M. Liu, S. Yazdi, J. Zhang, Q. Zhong, X. Zou, N. Zhao, H. Yu, Z. Jiang, E. Ringe, B. I. Yakobson, J. Dong, D. Chen and J. M. Tour, *ACS Nano*, 2017, **11**, 6930–6941.
106 H.-E. Kim, I. H. Lee, J. Cho, S. Shin, H. C. Ham, J. Y. Kim and H. Lee, *ChemElectroChem*, 2019, **6**, 4757–4764.
107 L. Jiao, J. Li, L. L. Richard, Q. Sun, T. Stracensky, E. Liu, M. T. Sougrati, Z. Zhao, F. Yang, S. Zhong, H. Xu, S. Mukerjee, Y. Huang, D. A. Cullen, J. H. Park, M. Ferrandon, D. J. Myers, F. Jaouen and Q. Jia, *Nat. Mater.*, 2021, **20**, 1385–1391.
108 W. Zhou, H. Su, Y. Li, M. Liu, H. Zhang, X. Zhang, X. Sun, Y. Xu, Q. Liu and S. Wei, *ACS Energy Lett.*, 2021, **6**, 3359–3366.
109 L. Bai, Z. Duan, X. Wen, R. Si and J. Guan, *Appl. Catal., B*, 2019, **257**, 117930.
110 X. Xie, L. Peng, H. Yang, G. I. N. Waterhouse, L. Shang and T. Zhang, *Adv. Mater.*, 2021, **33**, e2101038.
111 Q. Wang, R. Lu, Y. Yang, X. Li, G. Chen, L. Shang, L. Peng, D. Sun-Waterhouse, B. C. C. Cowie, X. Meng, Y. Zhao, T. Zhang and G. I. N. Waterhouse, *Sci. Bull.*, 2022, **67**, 1264–1273.
112 Z. Li, S. Ji, C. Xu, L. Leng, H. Liu, J. H. Horton, L. Du, J. Gao, C. He, X. Qi, Q. Xu and J. Zhu, *Adv. Mater.*, 2023, **35**, e2209644.
113 X. Shu, Q. Chen, M. Yang, M. Liu, J. Ma and J. Zhang, *Adv. Energy Mater.*, 2022, **13**, 2202871.
114 J. Zhang, H. Yang and B. Liu, *Adv. Energy Mater.*, 2021, **11**, 2002473.
115 Y. Lin, P. Liu, E. Velasco, G. Yao, Z. Tian, L. Zhang and L. Chen, *Adv. Mater.*, 2019, **31**, e1808193.
116 R. Jiang, L. Li, T. Sheng, G. Hu, Y. Chen and L. Wang, *J. Am. Chem. Soc.*, 2018, **140**, 11594–11598.
117 L. Yang, L. Shi, D. Wang, Y. Lv and D. Cao, *Nano Energy*, 2018, **50**, 691–698.
118 P. Yin, T. Yao, Y. Wu, L. Zheng, Y. Lin, W. Liu, H. Ju, J. Zhu, X. Hong, Z. Deng, G. Zhou, S. Wei and Y. Li, *Angew. Chem., Int. Ed.*, 2016, **55**, 10800–10805.
119 H. Jiang, J. Xia, L. Jiao, X. Meng, P. Wang, C.-S. Lee and W. Zhang, *Appl. Catal., B*, 2022, **310**, 121352.
120 Y. Qu, Z. Li, W. Chen, Y. Lin, T. Yuan, Z. Yang, C. Zhao, J. Wang, C. Zhao, X. Wang, F. Zhou, Z. Zhuang, Y. Wu and Y. Li, *Nat. Catal.*, 2018, **1**, 781–786.
121 R. Jasinski, *Nature*, 1964, **201**, 1212–1213.
122 H. Wang, Q. He, S. Liang, Y. Li, X. Zhao, L. Mao, F. Zhan and L. Chen, *Energy Storage Mater.*, 2021, **43**, 531–578.
123 X. Jiang, H. Li, J. Xiao, D. Gao, R. Si, F. Yang, Y. Li, G. Wang and X. Bao, *Nano Energy*, 2018, **52**, 345–350.
124 K. S. Park, Z. Ni, A. P. Côté, J. Y. Choi, R. Huang, F. J. Uribe-Romo, H. K. Chae, M. O'Keeffe and O. M. Yaghi, *Proc. Natl. Acad. Sci. U. S. A.*, 2006, **103**, 10186–10191.
125 C. C. Hou, L. Zou, L. Sun, K. Zhang, Z. Liu, Y. Li, C. Li, R. Zou, J. Yu and Q. Xu, *Angew. Chem., Int. Ed.*, 2020, **59**, 7384–7389.
126 B. Lu, T. J. Smart, D. Qin, J. E. Lu, N. Wang, L. Chen, Y. Peng, Y. Ping and S. Chen, *Chem. Mater.*, 2017, **29**, 5617–5628.
127 L. Yang, D. Cheng, H. Xu, X. Zeng, X. Wan, J. Shui, Z. Xiang and D. Cao, *Proc. Natl. Acad. Sci. U. S. A.*, 2018, **115**, 6626–6631.
128 K. Liu, G. Wu and G. Wang, *J. Phys. Chem. C*, 2017, **121**, 11319–11324.
129 N. Zhang, T. Zhou, M. Chen, H. Feng, R. Yuan, C. a. Zhong, W. Yan, Y. Tian, X. Wu, W. Chu, C. Wu and Y. Xie, *Energy Environ. Sci.*, 2020, **13**, 111–118.
130 J. H. Zagal and M. T. M. Koper, *Angew. Chem., Int. Ed.*, 2016, **55**, 14510–14521.
131 A. J. Medford, A. Vojvodic, J. S. Hummelshøj, J. Voss, F. Abild-Pedersen, F. Studt, T. Bligaard, A. Nilsson and J. K. Nørskov, *J. Catal.*, 2015, **328**, 36–42.
132 H. Shen, E. Gracia-Espino, J. Ma, H. Tang, X. Mamat, T. Wagberg, G. Hu and S. Guo, *Nano Energy*, 2017, **35**, 9–16.
133 P. Song, Y. Wang, J. Pan, W. Xu and L. Zhuang, *J. Catal.*, 2015, **300**, 279–284.
134 Q. Lai, L. Zheng, Y. Liang, J. He, J. Zhao and J. Chen, *ACS Catal.*, 2017, **7**, 1655–1663.
135 M. Xiao, Z. Xing, Z. Jin, C. Liu, J. Ge, J. Zhu, Y. Wang, X. Zhao and Z. Chen, *Adv. Mater.*, 2020, **32**, e2004900.
136 G. Chen, Y. An, S. Liu, F. Sun, H. Qi, H. Wu, Y. He, P. Liu, R. Shi, J. Zhang, A. Kuc, U. Kaiser, T. Zhang, T. Heine, G. Wu and X. Feng, *Energy Environ. Sci.*, 2022, **15**, 2619–2628.
137 Y. Mun, S. Lee, K. Kim, S. Kim, S. Lee, J. W. Han and J. Lee, *J. Am. Chem. Soc.*, 2019, **141**, 6254–6262.
138 L. Gong, H. Zhang, Y. Wang, E. Luo, K. Li, L. Gao, Y. Wang, Z. Wu, Z. Jin, J. Ge, Z. Jiang, C. Liu and W. Xing, *Angew. Chem., Int. Ed.*, 2020, **59**, 13923–13928.
139 X. X. Wang, V. Prabhakaran, Y. He, Y. Shao and G. Wu, *Adv. Mater.*, 2019, **31**, e1805126.
140 Z. Liang, H. Zheng and R. Cao, *Sustainable Energy Fuels*, 2020, **4**, 3848–3870.

141 P. Vasudevan, Santosh, N. Mann and S. Tyagi, *Transition Met. Chem.*, 1990, **15**, 81–90.
142 M. Yuasa, A. Yamaguchi, H. Itsuki, K. Tanaka, M. Yamamoto and K. Oyaizu, *Chem. Mater.*, 2005, **17**, 4278–4281.
143 Q. Cheng, L. Yang, L. Zou, Z. Zou, C. Chen, Z. Hu and H. Yang, *ACS Catal.*, 2017, **7**, 6864–6871.
144 X. Han, X. Ling, Y. Wang, T. Ma, C. Zhong, W. Hu and Y. Deng, *Angew. Chem., Int. Ed.*, 2019, **58**, 5359–5364.
145 J. Zhang, J. Yang, Y. Wang, H. Lu and M. Zhang, *Int. J. Energy Res.*, 2021, **45**, 10858–10868.
146 Y. Wang, K. Liu, J. Li, X. Yang, J. Hu, T.-S. Chan, X. Qiu, W. Li and M. Liu, *Chem. Eng. J.*, 2022, **429**, 132119.
147 X. Sun, S. Sun, S. Gu, Z. Liang, J. Zhang, Y. Yang, Z. Deng, P. Wei, J. Peng, Y. Xu, C. Fang, Q. Li, J. Han, Z. Jiang and Y. Huang, *Nano Energy*, 2019, **61**, 245–250.
148 S. Kattel, P. Atanassov and B. Kiefer, *Phys. Chem. Chem. Phys.*, 2013, **15**, 148–153.
149 R. Chen, H. Li, D. Chu and G. Wang, *J. Phys. Chem. C*, 2009, **113**, 20689–20697.
150 T. S. Olson, S. Pylypenko, P. Atanassov, K. Asazawa, K. Yamada and H. Tanaka, *J. Phys. Chem. C*, 2010, **114**, 5049–5059.
151 C. Médard, M. Lefèvre, J. P. Dodelet, F. Jaouen and G. Lindbergh, *Electrochim. Acta*, 2006, **51**, 3202–3213.
152 X. Sun, K. Li, C. Yin, Y. Wang, M. Jiao, F. He, X. Bai, H. Tang and Z. Wu, *Carbon*, 2016, **108**, 541–550.
153 J. Zhang, Y. Wang, Y. Wang and M. Zhang, *J. Electrochem. Soc.*, 2017, **164**, F1122–F1129.
154 Y. Liu, Y. Shen, L. Sun, J. Li, C. Liu, W. Ren, F. Li, L. Gao, J. Chen, F. Liu, Y. Sun, N. Tang, H.-M. Cheng and Y. Du, *Nat. Commun.*, 2016, **7**, 10921.
155 H. B. Yang, J. Miao, S.-F. Hung, J. Chen, H. B. Tao, X. Wang, L. Zhang, R. Chen, J. Gao, H. M. Chen, L. Dai and B. Liu, *Sci. Adv.*, 2016, **2**, e1501122.
156 X. Liu, Y. Zhang, Z. Zhao, H. Gao, J. Kang, R. Wang, G. Ge and X. Jia, *J. Mater. Chem. A*, 2021, **9**, 22643–22652.
157 X. Xu, X. Yan, Z. Zhong, L. Kang and J. Yao, *Carbon*, 2019, **145**, 311–320.
158 C. Fu, L. Luo, L. Yang, S. Shen, X. Yan, J. Yin, G. Wei and J. Zhang, *ChemCatChem*, 2021, **13**, 2303–2310.
159 G.-L. Chai, K. Qiu, M. Qiao, M.-M. Titirici, C. Shang and Z. Guo, *Energy Environ. Sci.*, 2017, **10**, 1186–1195.
160 J. Zhang and L. Dai, *Angew. Chem., Int. Ed.*, 2016, **55**, 13296–13300.
161 Z. Jiang, X. Zhao, X. Tian, L. Luo, J. Fang, H. Gao and Z.-J. Jiang, *ACS Appl. Mater. Interfaces*, 2015, **7**, 19398–19407.
162 X. Xu, S. Wang, S. Guo, K. San Hui, J. Ma, D. A. Dinh, K. N. Hui, H. Wang, L. Zhang and G. Zhou, *Adv. Powder Mater.*, 2022, **1**, 100027.
163 E. Jung, H. Shin, B. H. Lee, V. Efremov, S. Lee, H. S. Lee, J. Kim, W. Hooch Antink, S. Park, K. S. Lee, S. P. Cho, J. S. Yoo, Y. E. Sung and T. Hyeon, *Nat. Mater.*, 2020, **19**, 436–442.
164 B. Q. Li, C. X. Zhao, J. N. Liu and Q. Zhang, *Adv. Mater.*, 2019, **31**, e1808173.
165 H. Shen, N. Qiu, L. Yang, X. Guo, K. Zhang, T. Thomas, S. Du, Q. Zheng, J. P. Attfield, Y. Zhu and M. Yang, *Small*, 2022, **18**, e2200730.
166 Y. Zheng, D.-S. Yang, J. M. Kweun, C. Li, K. Tan, F. Kong, C. Liang, Y. J. Chabal, Y. Y. Kim, M. Cho, J.-S. Yu and K. Cho, *Nano Energy*, 2016, **30**, 443–449.
167 S. Zhang, H. Xue, W. L. Li, J. Sun, N. Guo, T. Song, H. Dong, J. Zhang, X. Ge, W. Zhang and Q. Wang, *Small*, 2021, **17**, e2102125.
168 H. Su, W. Zhou, H. Zhang, W. Zhou, X. Zhao, Y. Li, M. Liu, W. Cheng and Q. Liu, *J. Am. Chem. Soc.*, 2020, **142**, 12306–12313.
169 H. J. Qiu, P. Du, K. Hu, J. Gao, H. Li, P. Liu, T. Ina, K. Ohara, Y. Ito and M. Chen, *Adv. Mater.*, 2019, **31**, e1900843.
170 Z. Liang, M. Luo, M. Chen, X. Qi, J. Liu, C. Liu, S. G. Peera and T. Liang, *J. Mater. Chem. A*, 2020, **8**, 20453–20462.
171 M. S. Thorum, J. Yadav and A. A. Gewirth, *Angew. Chem., Int. Ed.*, 2009, **48**, 165–167.
172 Y. Xiao and W. Zhang, *SN Appl. Sci.*, 2020, **2**, 194.
173 S. Ma, Z. Han, K. Leng, X. Liu, Y. Wang, Y. Qu and J. Bai, *Small*, 2020, **16**, e2001384.
174 T. Sun, Y. Li, T. Cui, L. Xu, Y. G. Wang, W. Chen, P. Zhang, T. Zheng, X. Fu, S. Zhang, Z. Zhang, D. Wang and Y. Li, *Nano Lett.*, 2020, **20**, 6206–6214.
175 G. Han, X. Zhang, W. Liu, Q. Zhang, Z. Wang, J. Cheng, T. Yao, L. Gu, C. Du, Y. Gao and G. Yin, *Nat. Commun.*, 2021, **12**, 6335.
176 H. Wu, H. Li, X. Zhao, Q. Liu, J. Wang, J. Xiao, S. Xie, R. Si, F. Yang, S. Miao, X. Guo, G. Wang and X. Bao, *Energy Environ. Sci.*, 2016, **9**, 3736–3745.
177 P. Li, Z. Jin, Y. Qian, Z. Fang, D. Xiao and G. Yu, *Mater. Today*, 2020, **35**, 78–86.
178 K. Gong, F. Du, Z. Xia, M. Durstock and L. Dai, *Science*, 2009, **323**, 760–764.
179 Z. Shi and J. Zhang, *J. Phys. Chem. C*, 2007, **111**, 7084–7090.
180 X. Xie, J. Liu, T. Li, Y. Song and F. Wang, *Chemistry*, 2018, **24**, 9968–9975.
181 J. Hu, X. Cai, J. Wu, C. Xin, J. Guo, Z. Liu, J. Wei, X. Cheng, C. Hao, H. Dong, G. Zhang, N. Wang, Y. Lei, W. Liu and Y. Shi, *Chem. Eng. J.*, 2022, **430**, 133105.
182 H. Shang, X. Zhou, J. Dong, A. Li, X. Zhao, Q. Liu, Y. Lin, J. Pei, Z. Li, Z. Jiang, D. Zhou, L. Zheng, Y. Wang, J. Zhou, Z. Yang, R. Cao, R. Sarangi, T. Sun, X. Yang, X. Zheng, W. Yan, Z. Zhuang, J. Li, W. Chen, D. Wang, J. Zhang and Y. Li, *Nat. Commun.*, 2020, **11**, 3049.
183 J. Li, S. Chen, N. Yang, M. Deng, S. Ibraheem, J. Deng, J. Li, L. Li and Z. Wei, *Angew. Chem., Int. Ed.*, 2019, **58**, 7035–7039.
184 Z. Chen, W. Gong, Z. Liu, S. Cong, Z. Zheng, Z. Wang, W. Zhang, J. Ma, H. Yu, G. Li, W. Lu, W. Ren and Z. Zhao, *Nano Energy*, 2019, **60**, 394–403.
185 G. Zhu, F. Liu, Y. Wang, Z. Wei and W. Wang, *Phys. Chem. Chem. Phys.*, 2019, **21**, 12826–12836.

186 Z. Lin, H. Huang, L. Cheng, Y. Yang, R. Zhang and Q. Chen, *ACS Sustainable Chem. Eng.*, 2019, **8**, 427–434.
187 H. Shang, W. Sun, R. Sui, J. Pei, L. Zheng, J. Dong, Z. Jiang, D. Zhou, Z. Zhuang, W. Chen, J. Zhang, D. Wang and Y. Li, *Nano Lett.*, 2020, **20**, 5443–5450.
188 H. Shang, Z. Jiang, D. Zhou, J. Pei, Y. Wang, J. Dong, X. Zheng, J. Zhang and W. Chen, *Chem. Sci.*, 2020, **11**, 5994–5999.
189 Y. Yang, K. Mao, S. Gao, H. Huang, G. Xia, Z. Lin, P. Jiang, C. Wang, H. Wang and Q. Chen, *Adv. Mater.*, 2018, **30**, e1801732.
190 J. Li, M. Chen, D. A. Cullen, S. Hwang, M. Wang, B. Li, K. Liu, S. Karakalos, M. Lucero, H. Zhang, C. Lei, H. Xu, G. E. Sterbinsky, Z. Feng, D. Su, K. L. More, G. Wang, Z. Wang and G. Wu, *Nat. Catal.*, 2018, **1**, 935–945.
191 E. Luo, H. Zhang, X. Wang, L. Gao, L. Gong, T. Zhao, Z. Jin, J. Ge, Z. Jiang, C. Liu and W. Xing, *Angew. Chem., Int. Ed.*, 2019, **58**, 12469–12475.
192 B. Zhu, K. Qiu, C. Shang and Z. Guo, *J. Mater. Chem. A*, 2015, **3**, 5212–5222.
193 J. A. Cowan, *BioMetals*, 2002, **15**, 225–235.
194 M. F. Dunn, J. A. Ramirez-Trujillo and I. Hernandez-Lucas, *Microbiology*, 2009, **155**, 3166–3175.
195 O. Y. Bisen and K. K. Nanda, *Appl. Mater. Today*, 2020, **21**, 100846.
196 S. Liu, Z. Li, C. Wang, W. Tao, M. Huang, M. Zuo, Y. Yang, K. Yang, L. Zhang, S. Chen, P. Xu and Q. Chen, *Nat. Commun.*, 2020, **11**, 938.
197 M. D. Bhatt, G. Lee and J. S. Lee, *J. Phys. Chem. C*, 2016, **120**, 26435–26441.
198 Y. Qin, H.-H. Wu, L. A. Zhang, X. Zhou, Y. Bu, W. Zhang, F. Chu, Y. Li, Y. Kong, Q. Zhang, D. Ding, Y. Tao, Y. Li, M. Liu and X. C. Zeng, *ACS Catal.*, 2018, **9**, 610–619.
199 Z. Lin, H. Huang, L. Cheng, W. Hu, P. Xu, Y. Yang, J. Li, F. Gao, K. Yang, S. Liu, P. Jiang, W. Yan, S. Chen, C. Wang, H. Tong, M. Huang, W. Zheng, H. Wang and Q. Chen, *Adv. Mater.*, 2021, **33**, e2107103.
200 S. Zhang, Y. Wu, Y.-X. Zhang and Z. Niu, *Sci. China: Chem.*, 2021, **64**, 1908–1922.
201 T. Wu, S. Li, S. Liu, W.-C. Cheong, C. Peng, K. Yao, Y. Li, J. Wang, B. Jiang, Z. Chen, Z. Chen, X. Wei and K. Wu, *Nano Res.*, 2022, **15**, 3980–3990.
202 Y. Xiong, W. Sun, P. Xin, W. Chen, X. Zheng, W. Yan, L. Zheng, J. Dong, J. Zhang, D. Wang and Y. Li, *Adv. Mater.*, 2020, **32**, 2000896.
203 T. Yang, F. Qin, S. Zhang, H. Rong, W. Chen and J. Zhang, *Chem. Commun.*, 2021, **57**, 2164–2167.
204 Y. Yang, F. Li, J. Chen, J. Fan and Q. Xiang, *ChemSusChem*, 2020, **13**, 1979–1985.
205 O. Y. Podyacheva, D. A. Bulushev, A. N. Suboch, D. A. Svintsitskiy, A. S. Lisitsyn, E. Modin, A. Chuvilin, E. Y. Gerasimov, V. I. Sobolev and V. N. Parmon, *ChemSusChem*, 2018, **11**, 3724–3727.
206 H. Liu, H. Rong and J. Zhang, *ChemSusChem*, 2022, **15**, e202200498.
207 N. Du, C. Wang, R. Long and Y. Xiong, *Nano Res.*, 2017, **10**, 3228–3237.
208 L. Chong, J. Wen, J. Kubal, F. G. Sen, J. Zou, J. Greeley, M. Chan, H. Barkholtz, W. Ding and D.-J. Liu, *Science*, 2018, **362**, 1276–1281.
209 L. Zhang, J. Fischer, Y. Jia, X. Yan, W. Xu, X. Wang, J. Chen, D. Yang, H. Liu, L. Zhuang, M. Hankel, D. J. Searles, K. Huang, S. Feng, C. L. Brown and X. Yao, *J. Am. Chem. Soc.*, 2018, **140**, 10757–10763.
210 B. Hammer and J. K. Nørskov, *Adv. Catal.*, 2000, **45**, 71–129.
211 C. Wang, L. Kuai, W. Cao, H. Singh, A. Zakharov, Y. Niu, H. Sun and B. Geng, *Chem. Eng. J.*, 2021, **426**, 130749.
212 X. Zhong, S. Ye, J. Tang, Y. Zhu, D. Wu, M. Gu, H. Pan and B. Xu, *Appl. Catal., B*, 2021, **286**, 119891.
213 S. Gong, C. Wang, P. Jiang, L. Hu, H. Lei and Q. Chen, *J. Mater. Chem. A*, 2018, **6**, 13254–13262.
214 G. Yang, J. Zhu, P. Yuan, Y. Hu, G. Qu, B. A. Lu, X. Xue, H. Yin, W. Cheng, J. Cheng, W. Xu, J. Li, J. Hu, S. Mu and J. N. Zhang, *Nat. Commun.*, 2021, **12**, 1734.
215 B. Wang, J. Zou, X. Shen, Y. Yang, G. Hu, W. Li, Z. Peng, D. Banham, A. Dong and D. Zhao, *Nano Energy*, 2019, **63**, 103851.
216 L. Li, B. Chen, Z. Zhuang, J. Nie and G. Ma, *Chem. Eng. J.*, 2020, **399**, 125647.
217 X. Fang, L. Jiao, S. H. Yu and H. L. Jiang, *ChemSusChem*, 2017, **10**, 3019–3024.
218 Y. Ma, H. Fan, C. Wu, M. Zhang, J. Yu, L. Song, K. Li and J. He, *Carbon*, 2021, **185**, 526–535.
219 K. Khan, X. Yan, Q. Yu, S.-H. Bae, J. J. White, J. Liu, T. Liu, C. Sun, J. Kim, H.-M. Cheng, Y. Wang, B. Liu, K. Amine, X. Pan and Z. Luo, *Nano Energy*, 2021, **90**, 106488.
220 J. Mao, P. Liu, J. Li, J. Yan, S. Ye and W. Song, *J. Energy Chem.*, 2022, **73**, 240–247.
221 Z. Lu, B. Wang, Y. Hu, W. Liu, Y. Zhao, R. Yang, Z. Li, J. Luo, B. Chi, Z. Jiang, M. Li, S. Mu, S. Liao, J. Zhang and X. Sun, *Angew. Chem., Int. Ed.*, 2019, **58**, 2622–2626.
222 D. Liu, B. Wang, H. Li, S. Huang, M. Liu, J. Wang, Q. Wang, J. Zhang and Y. Zhao, *Nano Energy*, 2019, **58**, 277–283.
223 H. Cai, G. Zhang, X. Zhang, B. Chen, Z. Lu, H. Xu, R. Gao and C. Shi, *Small*, 2022, **18**, 2200911.
224 J. Wang, Z. Huang, W. Liu, C. Chang, H. Tang, Z. Li, W. Chen, C. Jia, T. Yao, S. Wei, Y. Wu and Y. Li, *J. Am. Chem. Soc.*, 2017, **139**, 17281–17284.
225 J. Bai, W. Ge, P. Zhou, P. Xu, L. Wang, J. Zhang, X. Jiang, X. Li, Q. Zhou and Y. Deng, *J. Colloid Interface Sci.*, 2022, **616**, 433–439.
226 H. Jin, J. Zhu, R. Yu, W. Li, P. Ji, L. Liang, B. Liu, C. Hu, D. He and S. Mu, *J. Mater. Chem. A*, 2022, **10**, 664–671.
227 Z. Chen, X. Su, J. Ding, N. Yang, W. Zuo, Q. He, Z. Wei, Q. Zhang, J. Huang and Y. Zhai, *Appl. Catal., B*, 2022, **308**, 121206.